

# Flow Distortion Measurements in Convolved Aero Engine Intakes

Pavlos K. Zachos<sup>1</sup>, David G. MacManus<sup>2</sup>, Daniel Gil Prieto<sup>3</sup> and Nicola Chiereghin<sup>4</sup>

*Propulsion Engineering Centre, School of Aerospace, Transport and Manufacturing, Cranfield University,  
Cranfield, MK43 0AL, United Kingdom*

The unsteady flowfields generated by convoluted aero-engine intakes are sources of instabilities that can compromise the performance of the downstream turbomachinery. Hence, there is a need for synchronous, high-spatial resolution measurements that will allow a greater understanding of the aerodynamics. In this work, Stereo Particle Image Velocimetry (S-PIV) is used in a new application to characterize the distorted flow at the outlet of complex intake. A suite of measurements and analyses for two S-duct configurations across a range of inlet Mach numbers are presented. The work demonstrates the feasibility of using S-PIV techniques for determining the flow field at the exit of convoluted intakes with a higher spatial resolution than typical pressure measurements. Analysis of the distortion descriptors quantifies the dependency upon the S-duct configuration and highlights that the more high-offset duct generates greater levels of swirl distortion relative to the low-offset configuration. Distortion maps show that the flow is highly unsteady with a characteristic switching of the swirling flow. The results provide a new dataset which shows that the conventional assessments based on time-averaged data substantially underestimates the swirl distortion level and that the less frequent distortion events give rise to more potentially significant threats to the compression system.

## Nomenclature

A = area

<sup>1</sup> Lecturer in Aerodynamics, Propulsion Engineering Centre, Cranfield University, M43 0AL, UK, AIAA Member.

<sup>2</sup> Senior Lecturer in Aerodynamics, Propulsion Engineering Centre, Cranfield University, M43 0AL, UK, AIAA Member.

<sup>3</sup> Doctoral Researcher, Propulsion Engineering Centre, Cranfield University, M43 0AL, UK.

<sup>4</sup> Doctoral Researcher, Propulsion Engineering Centre, Cranfield University, M43 0AL, UK.

1	$D$	=	diameter
2	$H$	=	offset
3	$k$	=	swirl pairs index
4	$L$	=	length
5	$m$	=	total number of swirl pairs
6	$p_0$	=	total pressure
7	$P_0$	=	area-averaged total pressure
8	$q$	=	dynamic head
9	$r, \theta, z$	=	cylindrical frame of reference
10	$Re_D$	=	diameter based Reynolds number
11	$u_r, u_\theta, w$	=	instantaneous velocities
12	$u'_r, u'_\theta, w'$	=	instantaneous velocity fluctuations
13	$U_r, U_\theta, W$	=	area averaged time averaged velocity components
14	$x, y, z$	=	Cartesian frame of reference
15			
16	<b>Subscripts</b>		
17	$avg, mean$	=	average
18	$i$	=	index i
19	$in$	=	inlet plane
20	$max$	=	maximum
21	$min$	=	minimum
22	$out$	=	exit plane
23	$ref$	=	reference value at the AIP
24	$rms$	=	root mean square
25	$std$	=	standard deviation
26			
27	<b>Operators</b>		
28	$\langle \rangle$	=	time average

$\sigma$  = standard deviation

### Greek symbols

$\alpha$  = swirl angle, degrees

$\rho$  = density, kg/m<sup>3</sup>

$\omega_z$  = out-of-plane vorticity, 1/s

## I. Introduction

WITH the drive towards shorter and more complex intakes for advanced propulsion system installations, the coupling between the intake and fan becomes more critical. Intake flow distortion can be particularly severe for convoluted ducts, which are relevant to close-coupled engine installation arrangements. This is of interest to a range of applications including future civil aircraft configurations which may feature novel propulsion integration configurations such as boundary layer ingestion or distributed electric propulsion<sup>1,2</sup>. Inlet distortion may be a critical design aspect for these configurations with unconventional intakes. Semi-immersed propulsion systems, as well as coreless fans in turbo-electric distributed propulsion architectures, were found to be susceptible to intake flow separations<sup>1,2</sup>. This results in complex total pressure and swirl flow fields, significant vortical regions and large unsteady flow perturbations at the Aerodynamic Interface Plane (AIP) downstream of the intake<sup>1,2,3-6</sup>. Total pressure and swirl distortions can be generated by flow separations within the intake that may result in low momentum flow regions or swirling flow which is either co- or contra-rotating with respect to the compression system and affects flow incidence onto the blade. As a result, complex unsteady total pressure and swirl flow fields are generated at the AIP, which, in turn, affects the flow capacity as well as the pressure rise and the surge margin of the compression system. Previous work showed that for a system with a total-pressure distortion, the introduction of co-rotating swirl, slightly decreased the stability margin compared to total-pressure distortion alone<sup>7</sup>. However, the combination of counter-rotating swirl with total-pressure distortion substantially reduced the stability margin. It has been observed that counter-rotating swirl in conjunction with total pressure distortion can completely consume the surge margin of the compression system<sup>7</sup>.

For the design of convoluted engine intakes, one of the design drivers is the minimization of the distortion that can result in a non-uniform distribution of swirl angle and total pressure across the AIP. This may adversely affect the engine stability or operation. The simulated time-averaged total pressure and swirl angle distributions across the

exit plane of a typical diffusing S-duct is shown in Fig. 1 as an example of the average flow non-uniformities that arise in such configurations and are presented at the AIP<sup>8</sup>. This illustrative example is from a computational fluid dynamics (CFD) study using a steady Reynolds Averaged Navier Stokes method<sup>8</sup>. For this example, the S-duct comprised an area ratio of  $A_{out}/A_{in} = 1.52$ , a vertical offset to inlet diameter ratio  $H/D_{in}$  of 1.34 and a length to inlet diameter ratio  $L/D_{in}$  of 5.0. Visualization of the computed streaklines on the duct surface showed a separated flow region that develops at the lower part of the duct. In addition, the overturning of the boundary layers is highlighted by the deviation of the surface streaklines due to the development of the classical secondary flows through the curved duct (Fig. 1a). This gives rise to the formation of two main counter-rotating vortical structures (Fig. 1b). In addition, these vortices exhibit notable levels of swirl variation of  $\pm 20^\circ$  across the AIP (Fig. 1c) as well as two clear foci in the lower sector of the plane. There is also a non-uniform distribution of total pressure with two local minima of total pressure ratio associated with the vortices (Fig. 1d). Crossflow plane measurements for the same configuration, and reported by Wellborn et al<sup>3</sup>, also showed that the time-averaged flow field comprised a pair of streamwise vortices at the outlet of the S-duct associated with a low pressure zone on the lower part of the plane. Such a simultaneous presence of total pressure and swirl distortion at the inlet of the compressor has previously been demonstrated to be a source of loss in surge margin, while it increases the possibility of stall inception<sup>7,9</sup>. High bandwidth pressure measurements in two S-duct geometries with offset to inlet diameter ratios ( $H/D_{in}$ ) of 1.34 and 2.44, respectively, highlighted a notable instability in the primary flow separation region<sup>4,5</sup>. This instability was found to produce oscillations of the flow distortions at the exit plane, which is an additional source of loss in performance and operability for the compression system<sup>10</sup>. For swirl distributions, almost no publicly available data exist to support the understanding of the underlying unsteady swirl distortion characteristics. However, from industrial experience, the need to consider swirl distributions during operability assessments is evident across a wide range of aircraft aero-engine applications<sup>7</sup>.

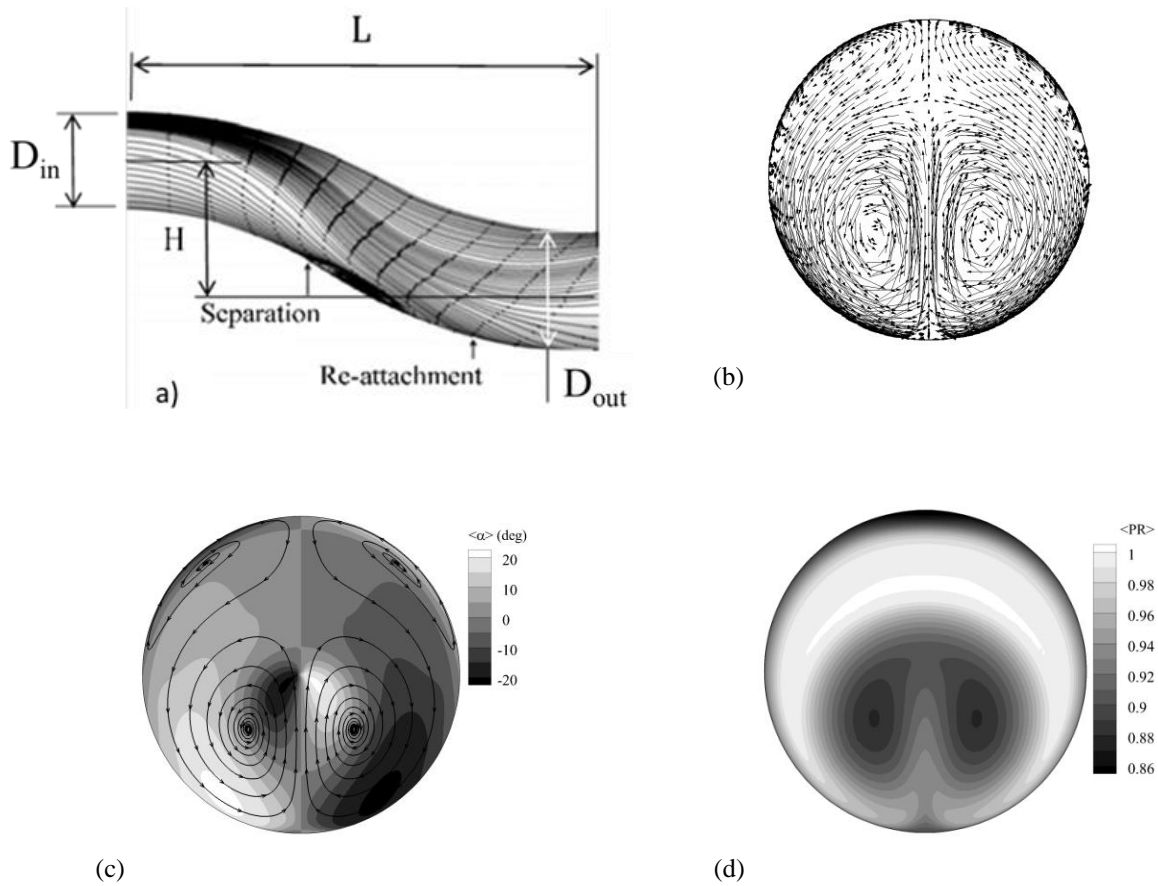


**Fig. 1 Example of the flow field for a convoluted S-duct calculated using a steady RANS simulation. (a) surface streaklines, (b) velocity vectors, (c) swirl angle distribution and in-plane streaklines, (d) total pressure ratio at the AIP <sup>8</sup>.**

From an industrial perspective, to systematically quantify the different kinds of distortion, various descriptors have been introduced by engine manufacturers and engineering bodies<sup>7,9,11,12</sup>. Current industry practice for the quantification of distorted flow fields for compressor or fan systems typically relies on steady state measurements from experimental tests which enables the characterization of distortion via the appropriate descriptors. For example, a conventional measurement arrangement for advanced engine intakes uses a total pressure rake at the AIP comprising an array of 8 spokes with 5 probes each<sup>7</sup>. These pressure measurements are then used to describe

distortion of total pressure in terms of reduced metrics for overall, circumferential and radial non-uniformities. A similar approach, with typically less spatial resolution, is adopted for total temperature and swirl non-uniformities. Although these low frequency, time-averaged measurements may be supplemented with a sub-set of unsteady pressure measurements, it is considered as being unable to capture the detailed unsteady behavior of the flow<sup>5,7,13,14</sup>. This is mainly due to its low spatial and temporal resolution that is insufficient to capture the complex nature of the generated flow fields. Nevertheless, a range of total pressure based distortion descriptors, such as the distortion coefficient which is based on the 60° sector with the greatest total pressure loss, DC(60), is typically considered. DC(60) is defined as the difference between the average total pressure,  $p_{0,avg}$ , and the lowest average total pressure in a sector of 60° angle,  $p_{60°,avg}$  and non-dimensionalized by the mean dynamic head  $q$  of the AIP<sup>15, 16</sup>.

$$DC(60) = \frac{p_{0,avg} - p_{60°,avg}}{q} \quad (1)$$

Relative to this conventional measurement approach, Stereoscopic Particle Image Velocimetry methods (S-PIV) has the potential to provide higher spatial resolution across a typical AIP measurement plane. Although S-PIV is a relatively mature measurement method, there has been no previous work that addresses the measurement of flow distortion across the full crossflow plane of an intake as considered in this work. This is a key requirement for inlet flow distortion assessments as the quantification of the distortion parameters depends on the measurements across the AIP. An additional benefit of the S-PIV measurements, applied at the AIP, is that it provides three-components of the velocity field in a synchronous manner. Therefore, the distortion metrics can be determined at each S-PIV snapshot and thereby provide an assessment of the statistical variation of the intake distortion metrics that are expected to be notably different from the conventional time-averaged distortion.

Although no previous S-PIV work has been successfully performed at the full AIP of a convoluted air intake, some previous studies are pertinent to this work<sup>17-20</sup>. Kalpakli et al<sup>17</sup> performed cross flow, time resolved S-PIV measurements at the exit plane of curved pipes. The measured unsteady flow data along with the development of a Proper Orthogonal Decomposition post processing approach was able to identify the underpinning vortical patterns and to indicate their origin. Previous experiments for cylindrical ducts with water<sup>18</sup>, proved the feasibility of S-PIV techniques to measure flows with large out-of-plane velocity components. Doorne et al<sup>18</sup> and Nelson et al<sup>19</sup> highlighted the complexities of performing S-PIV through cylindrical ducts and quantified some of the underlying challenges associated with it. These tests showed that the curved cylindrical walls of the test section cause additional

optical distortions that impose uncertainties onto the mapping functions especially close to the boundaries. These errors can be accounted for through a mis-registration correction algorithm. The importance of laser light management was also highlighted to avoid excessive secondary light scattering and reflections by the cylindrical walls which increase the measurement noise by up to 60%<sup>19,20</sup>. Within the context of flow distortion, Guimarães et al.<sup>21</sup> used S-PIV to characterize the swirl distorted pattern generated with complex swirl-generator screens. The evolution of the swirl pattern in front of a full-scale turbofan engine was investigated.

The aim of this paper is to use Stereoscopic Particle Image Velocimetry (S-PIV) to provide a notable improvement in the measurement and analysis of the distorted velocity and swirl flow field generated by a complex aero-engine intake. A bespoke test facility was designed and built to facilitate the installation of various convoluted intakes (S-ducts). The practical challenges associated with the application of this technique within confined, highly distorted internal flows are assessed along with aspects on the measurement uncertainties. Measurements are presented for two intake configurations of different vertical offset across a range of inlet Mach numbers. The steady and unsteady characteristics and distortion of the flow are studied through a statistical analysis of the key velocity parameters and swirl descriptors.

## II. Experimental Setup and Methods

### A. Experimental Facility

The experiments were conducted using a bespoke rig at Cranfield University<sup>22</sup> which was designed to accommodate a range of convoluted ducts and to allow good optical access to enable S-PIV measurements at the crossflow exit plane of the intake ducts. The general arrangement of the rig is shown in Fig. 2. The facility comprises a bell-mouth intake followed by a flow conditioning section of 200 mm diameter that contains a honeycomb mesh that is 100 mm long and with hexagonal cell sizes of 6 mm diagonal length. Aft of the intake throat and ahead of the honeycomb section, twelve static pressure tappings are equi-spaced circumferentially and, in conjunction with the intake reference total pressure, are used to determine the rig operating point. Downstream of the flow conditioner is a constant diameter section of 200 mm diameter which can accommodate a swirl distortion generator and then a conical nozzle section where the diameter reduces from 200 mm to 121.6 mm over a distance of 200 mm. The inlet of the convoluted ducts has a diameter of  $D_{in} = 121.6$  mm.

The test rig was designed in a modular way so that the installation of various S-duct geometries can be facilitated. Two convoluted ducts have been designed, manufactured and tested. Similar to the work of Wellborn<sup>3</sup> using an S-duct with a simple circular cross-section, the baseline configuration has an offset-to-diameter ratio of  $H/D_{in} = 1.34$ , a length to diameter ratio of  $L/D_{in} = 5$  and with an overall diffusing area ratio  $A_{out}/A_{in} = 1.52$  (Fig. 3). An S-duct with a higher offset has been also tested based on the work of Garnier et al<sup>5</sup> with a  $H/D_{in} = 2.44$ , a  $L/D_{in} = 4.95$  and with the same area ratio of  $A_{out}/A_{in} = 1.52$ . For this work, the diameter at the AIP is 150 mm for both configurations. This is similar to previous work that mostly focused on conventional steady and unsteady pressure measurements<sup>4,5</sup>. At the exit of the S-duct a borosilicate glass working section with an inner diameter of 150 mm and a length of 300 mm was used. The working section was linked to a retractable diffuser duct and ultimately to a single stage centrifugal fan.

At a location  $0.9D_{in}$  upstream of the duct inlet plane, the circumferential distribution of static pressure is measured using 6 equi-spaced pressure tapings. The total pressure profile was measured  $0.9D_{in}$  upstream of the S-duct inlet using a flattened boundary layer Pitot probe that has a dimension of 0.4 mm by 1.05 mm. The spatial resolution of the radial traverse was 0.5 mm. The total pressure profile, in combination with the circumferentially averaged static pressures, were used for the derivation of the inlet Mach number profile across the range of tunnel operating conditions. The inlet Mach number profile was reduced to an area-weighted reference Mach number. The uncertainty on the inlet Mach number was assessed by considering the uncertainty elements of the total and static pressure measurement transducer as well as the errors attributed to the measurement of ambient pressure and total temperature. The deterministic pressure measurement uncertainties comprise the transducer accuracy, the resolution uncertainty and the calibration uncertainty. The stochastic element was taken into account as the standard deviation of the sample mean value. The pressure measurements were acquired at a sampling rate of 1 kHz for 10 seconds. Using uncertainty propagation analysis<sup>23</sup>, the uncertainty on the inlet Mach number was calculated as  $0.27 \pm 0.004$  and  $0.6 \pm 0.002$  respectively.



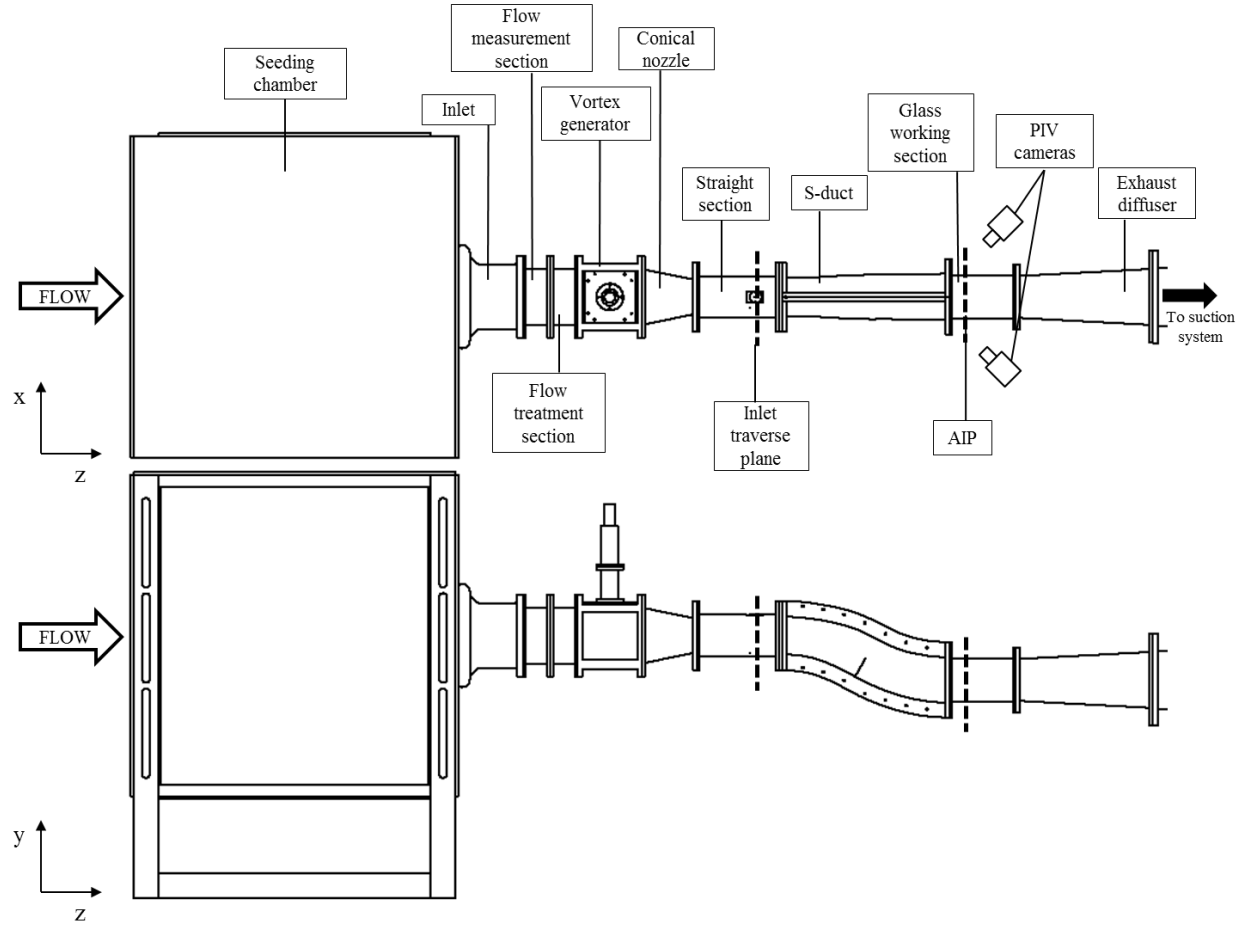


**Fig. 2 General arrangement of the test rig.**

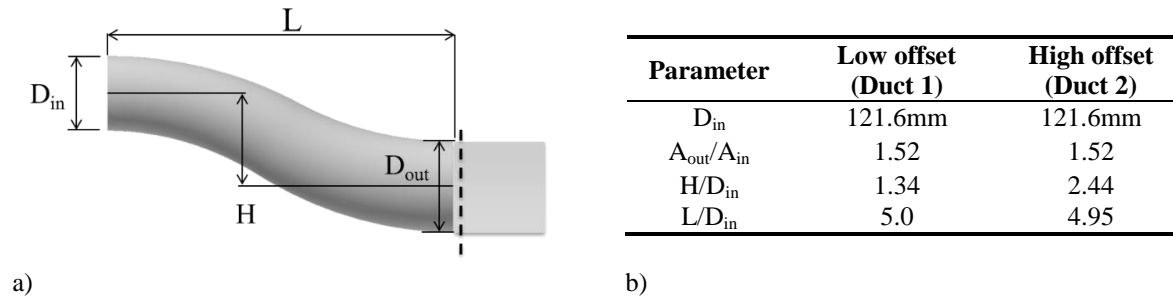


**Fig. 3 (a): Schematic definition of S-Duct parameters and (b): design parameters for the two S-duct configurations.**

## B. S-PIV Methods

The flow at the AIP was illuminated by a dual cavity frequency-doubled pulsed Nd:YAG laser with a maximum power of 200 mJ/pulse and an acquisition rate of 7.5 Hz. The amount of light used for the data acquisition was adjusted as required using a motorized attenuator. The laser light sheet was delivered by an articulated light arm, which combines a series of optics to convert the incoming laser beam into a thin light sheet that was adjusted to cover the full AIP area. The delivered laser light sheet had an estimated thickness of 1.5mm. The laser arm was mounted onto a positioning system that allowed the light sheet to be translated laterally and parallel to the rig axis as well as to be rotated about the two axes. This arrangement allowed for exact positioning and control of the light sheet within the region of interest.

Two TSI PowerView Plus cameras were used in a stereoscopic partial side scatter configuration with an approximately 45° off-axis arrangement (see Fig. 2). The cameras had a 4MP square sensor with an image resolution of 2048 x 2048 pixel (px). A pair of AF 1.8/D Nikkor lenses was used with a focal length of 50 mm and the cameras were positioned with a stand-off distance of approximately 600 mm. The camera mounts featured a coarse and a fine 2-axis positioning system that allows the positioning of the cameras along the x-z plane. The cameras were positioned along the AIP centreline and therefore the camera alignment and imaging was facilitated by a planar Scheimpflug mechanism. The camera aperture, focus and Scheimpflug setting were all remotely controlled.

Di-Ethyl-Hexyl Sebacate (DEHS) was used for the seeding of the flow. The seeding particles were generated by a Laskin nozzle particle generator. A 10 bar 860-liter pressure vessel was used to feed the seeder with the required airflow for the duration of the tests. The air-seeding mixture was pre-conditioned in a bespoke seeding chamber. The chamber had four solid walls and two open surfaces that each feature a double layer of turbulence mesh. The meshes are designed so that the wires of the external layer generate turbulent flow that is expected to enhance the mixing process while the inner layer damps the flow turbulence levels to provide a homogenous air-seeding cloud which is subsequently ingested by the rig. The turbulence grids are designed based on the guidelines provided by Roach<sup>24</sup>.

The camera spatial calibration at the region of interest was performed using a calibration target featuring a rectangular grid of 10 mm spaced dots with a 2 mm diameter. The target plate was placed in the glass working section and the multi plane calibration was performed using a translation along the z-axis of the working section. A five plane calibration was used with an inter-plane spacing along the z axis of 0.375 mm.

### C. Image Processing and Vector Evaluation

The evaluation of the S-PIV images is performed using the TSI InSight4G software. The workflow comprises image pre-processing to subtract the background from all the individual images, two-pass image cross-correlation and finally post-processing and vector validation. Third order image dewarping polynomials were generated based on the calibration target. A recursive Nyquist grid was used as a grid engine for the cross-correlation. The cross correlation engine was a Fast Fourier Transform correlator. The first cross-correlation pass was made with 64 px x 64 px interrogation areas. A 5 px x 5 px vector validation was applied before the second cross-correlation pass on 32 px x 32 px interrogation areas. The window overlap was set to 50% which yielded a 1.2 mm x 1.2 mm spatial resolution after the second pass. The signal to noise filter was set to 1.8. The number of spurious vectors after the second pass validation and smoothing process was less than 10% of the overall velocity vectors. After the final vector smoothing pass a flow field comprising approximately 9,000 velocity vectors is obtained at the AIP which corresponds to a resolution of 0.8% of the AIP diameter in both x and y direction.

The reconstruction of the velocity vectors from the two off-axis image recordings contain potential errors that originate from the misalignment between the calibration target and the laser light sheet (image mis-registration errors)<sup>25</sup>. Within the current study these errors were accounted for by calculating the disparity maps and correcting the calibration polynomials accordingly. The disparity processing was iteratively done in multiple passes using the entire dataset of images. The mean mis-registration error after multiple disparity corrections was typically around 3 px except for the regions very close to the walls where the mis-registration was estimated up to 5 px due to local laser light scattering effects. The analysis of Raffel<sup>25</sup> was followed to provide an estimate of the overall S-PIV uncertainties. This analysis takes into account the particle image displacement, particle image diameter, the seeding density the quantization level and the background noise. The overall uncertainty on the measured in-plane velocity was 4% and 8% on the out-of-plane velocity.

## III. Results and Discussion

### A. Time Averaged and Unsteady Flow Analysis

The test matrix of the flow measurements is shown in Table 1 where the S-duct inlet Mach number ranged from 0.27 to 0.60. The change in Mach number caused a concomitant variation of the inlet diameter based Reynolds number ( $Re_D$ ), which ranged from  $5.9 \times 10^5$  to  $13.8 \times 10^5$ . For the calculation of the inlet Mach number, the Mach number profile measured at the inlet reference plane located  $0.9D_{in}$  upstream the S-Duct inlet was an area weighted

averaged to account for the boundary layer regions. Using this upstream Mach number profile and the inlet total temperature, the velocity profile was determined and the incoming compressible boundary layer displacement thickness, momentum thickness and shape factor were calculated for the two configurations across a range of  $M_{in}$  between 0.27 - 0.6. The inlet boundary layer upstream of the S-duct inlet had a thickness ranging from 8.5 mm to 7.4 mm across the Mach number range and the displacement thickness reduced from approximately 1.2 mm to 1.1 mm between inlet Mach 0.27 and 0.6. The shape factor ranged between 1.5 to 1.7 and it was assumed the incoming boundary layer was fully turbulent.

For the S-PIV measurements, the time-averaged flow fields and statistical characteristics were calculated using 1000 flow snapshots that were acquired at 7.5 Hz. It is of interest to understand for this dynamic flow field if this is a sufficient dataset. Fig. 4 shows the non-dimensional time averaged out-of-plane velocity,  $\langle w \rangle / W_{ref}$ , and its fluctuations,  $\sigma_w$ , for datasets of 250, 500, 750, 1000 and 2000 PIV snapshots for the low offset S-duct at  $M_{in}=0.27$ . The data is non-dimensionalized by a reference out-of-plane velocity  $W_{ref} = \frac{1}{A} \int_A \langle w(r, \theta, t) \rangle dA$  which is the area-averaged, time-averaged out-of-plane velocity at the AIP. The impact of the number of snapshots on the non-dimensional, area and time averaged out-of-plane velocity  $W/W_{ref}$  and its non-dimensional, area averaged standard deviation  $\sigma_w/W_{ref}$  is shown in Fig. 5. Relative to the data taken with 1000 snapshots, the results for 2000 snapshots show that the change in  $W/W_{ref}$  was approximately 0.0% and within 0.6% for  $\sigma_w/W_{ref}$ . Similar convergence studies were conducted for the high offset case (Duct 2) and the adequacy of 1000 images per dataset was established as the characteristics for the out-of-plane velocity ( $W/W_{ref}$ ) converged within 0.11% and 0.8% for  $\sigma_w/W_{ref}$  between 1000 and 2000 snapshots. Therefore, for this work 1000 instantaneous images are considered adequate.

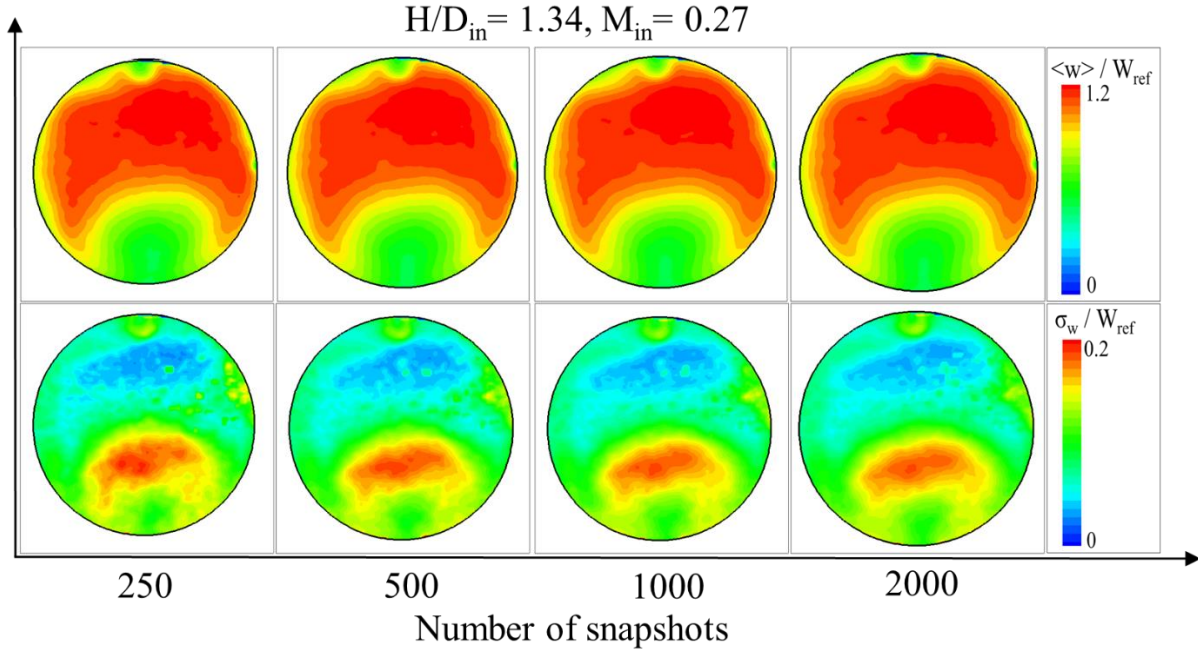


**Fig. 4** Effect of number of S-PIV snapshots on spatial distributions of  $\langle w \rangle / W_{\text{ref}}$  and  $\sigma_w / W_{\text{ref}}$  for Duct 1 ( $H/D_{\text{in}} = 1.34$ ) at  $M_{\text{in}} = 0.27$ .

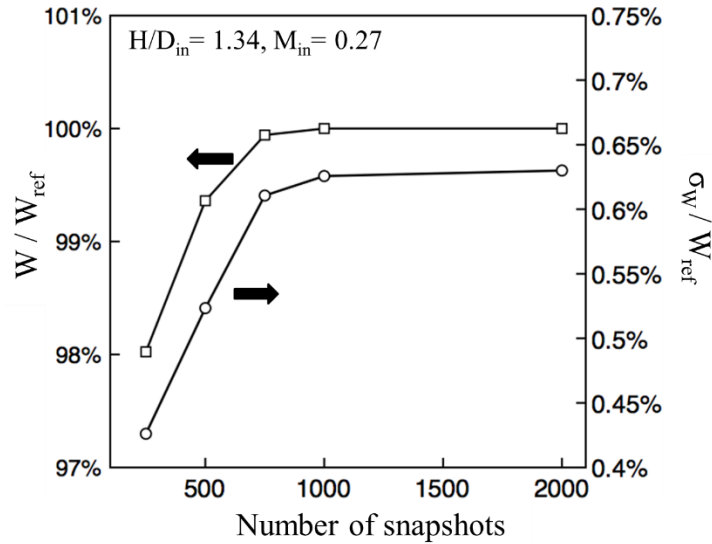


**Fig. 5** Effect of number of snapshots on  $W / W_{\text{ref}}$  and  $\sigma_w / W_{\text{ref}}$  for Duct 1 ( $H/D_{\text{in}} = 1.34$ ) at  $M_{\text{in}} = 0.27$ .

For the test configurations considered, the statistics of the non-dimensional velocity components, swirl angle, and turbulent kinetic energy were calculated at the AIP for the lowest and highest inlet Mach number cases. The anticipated low velocity region appears in both configurations as shown in Fig. 6. In accordance with previous

studies<sup>3-5</sup> this low velocity region is more pronounced for the high offset configuration ( $H/D_{in}=2.44$ ) in comparison with the low offset Duct 1 ( $H/D_{in}=1.34$ ). The increase in the extent of the low velocity region is related to both the stronger classical secondary flows, which arise in the high offset configuration as well as the expected upstream movement of the centreline separation point<sup>26</sup>. In addition, these stronger secondary flows for the high-offset Duct 2 ( $H/D_{in}=2.44$ ) also result in a radial migration of the main loss region to a more central location AIP. This is important as it is known that the conventional flow distortion descriptors, and the compression systems, are sensitive to the radial position of the flow distortions<sup>7,11</sup>. In addition, previous measurements of the area-averaged total pressure distributions at the AIP showed that the high offset configuration had a greater pressure loss with a pressure recovery ( $PR = P_{0, AIP} / P_{0, in}$ ) of 0.952 relative to 0.971 for the low offset Duct 1<sup>4,5</sup>. Finally, the inlet Mach number, and the associated changes in Reynolds number across the range of  $0.6 \times 10^6$  to  $1.4 \times 10^6$ , does not have a strong effect on the non-dimensional out-of-plane velocity distributions (Fig. 6). There is a modest, but noticeable, effect whereby the circumferential extent of the low velocity region is slightly reduced when the Mach number is increased from 0.27 to 0.6 (Fig. 6). This may be associated with the increase in Reynolds number and the concomitant reduction in the boundary layers which form into the secondary flow loss regions.

**Table 1 Test matrix for S-PIV tests.**

Case no.	Duct type	Inlet $Re_D$	Area averaged $M_{in}$
1	<u>Duct 1</u>	$5.9 \times 10^5$	0.27
2	$H/D_{in} = 1.34$	$9.9 \times 10^5$	0.45
3	$L/D_{in} = 5.0$	$13.2 \times 10^5$	0.6
4	<u>Duct 2</u>	$6.0 \times 10^5$	0.27
5	$H/D_{in} = 2.44$	$10.1 \times 10^5$	0.45
6	$L/D_{in} = 4.95$	$13.8 \times 10^5$	0.6

A key concern in the assessment of intake flow distortion is the lack of knowledge on the unsteady characteristics of the distortion metrics and the nature of the unsteady velocity field. Major differences in the unsteadiness characteristics are observed between the two geometries when the non-dimensional offset is  $H/D_{in}$  is increased from 1.34 to 2.44 (Fig. 7 to Fig. 10). For the low offset configuration (Duct 1,  $H/D_{in}=1.34$ ) the distribution of the out-of-plane velocity fluctuation  $\sigma_w/W_{ref}$  shows a local maximum of about 0.18 (Fig. 7) which is positioned at the top of the loss region highlighted in the time averaged non-dimensional  $w$  velocity distributions of Fig. 6. There

is also a local maximum of  $\sigma_w/W_{ref}=0.10$  at the top of the AIP plane which is associated with the minor local loss in this region. As the Mach number increases from 0.27 to 0.60 these characteristics are broadly unaffected (Fig. 7). There is a notable change in the unsteady  $\sigma_w/W_{ref}$  fluctuation for the high offset configuration (Duct 2,  $H/D_{in}=2.44$ ) (Fig. 7). The clearest change is that the region of peak unsteadiness is more extensive, with greater peak values (0.20) and located in a more central position. However, it has some similarities with the  $H/D_{in}=1.34$  configuration in that the main region of  $\sigma_w/W_{ref}$  is also associated with the upper extent of the main loss zone. The other characteristic associated with the high offset Duct 2, is that there is no longer an extensive region of substantially low  $\sigma_w/W_{ref}$  and that the levels are generally higher across the AIP. An increase in Mach number from 0.27 to 0.6 does not notably change the topology of  $\sigma_w/W_{ref}$  for Duct 2 (Fig. 7).

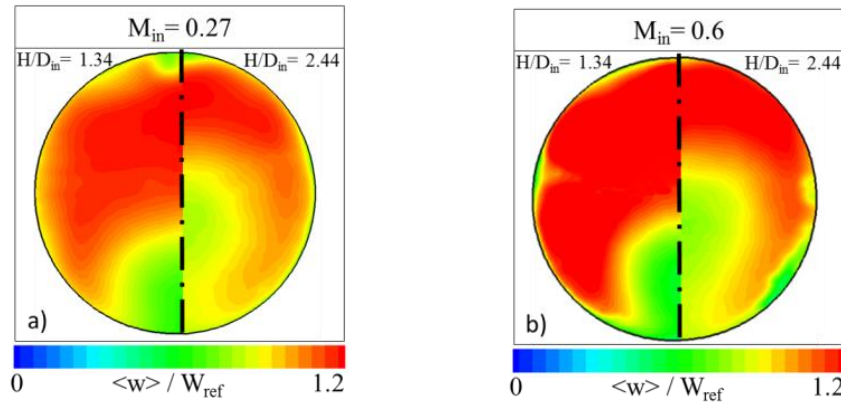


**Fig. 6 Non-dimensional time averaged out-of-plane velocity  $\langle w \rangle / W_{ref}$  at the AIP. (a-left):  $H/D_{in} = 1.34$ ,  $M_{in} = 0.27$ , (a-right):  $H/D_{in} = 2.44$ ,  $M_{in} = 0.27$ , (b-left):  $H/D_{in} = 1.34$ ,  $M_{in} = 0.6$ , (b-right):  $H/D_{in} = 2.44$ ,  $M_{in} = 0.6$ .**

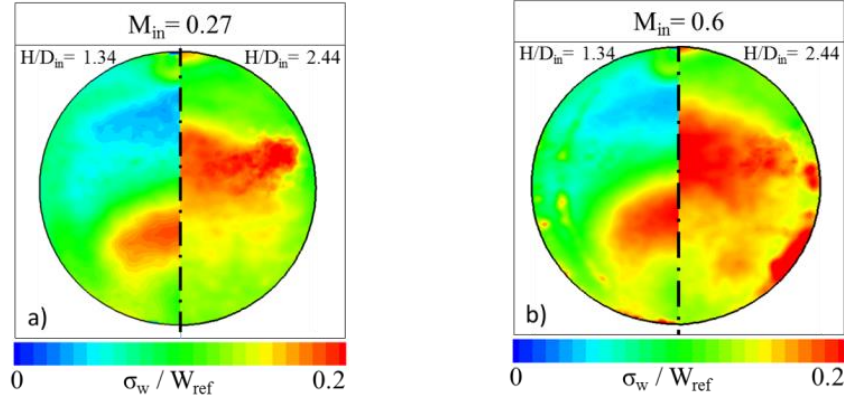


**Fig. 7** Non-dimensional out-of-plane velocity fluctuations  $\sigma_w / W_{ref}$  at the AIP. (a-left):  $H/D_{in} = 1.34$ ,  $M_{in} = 0.27$ , (a-right):  $H/D_{in} = 2.44$ ,  $M_{in} = 0.27$ , (b-left):  $H/D_{in} = 1.34$ ,  $M_{in} = 0.6$ , (b-right):  $H/D_{in} = 2.44$ ,  $M_{in} = 0.6$ .

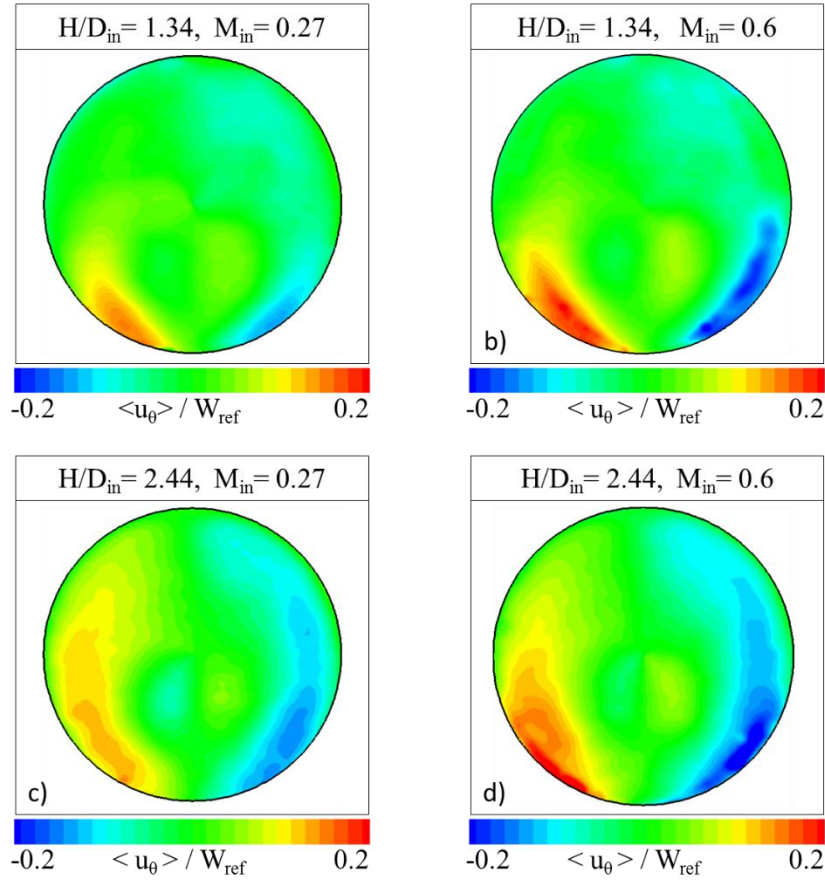


**Fig. 8** Non-dimensional time averaged circumferential velocity  $\langle u_\theta \rangle / W_{ref}$  at the AIP. (a):  $H/D_{in} = 1.34$ ,  $M_{in} = 0.27$ , (b):  $H/D_{in} = 1.34$ ,  $M_{in} = 0.6$ , (c):  $H/D_{in} = 2.44$ ,  $M_{in} = 0.27$ , (d):  $H/D_{in} = 2.44$ ,  $M_{in} = 0.6$ .



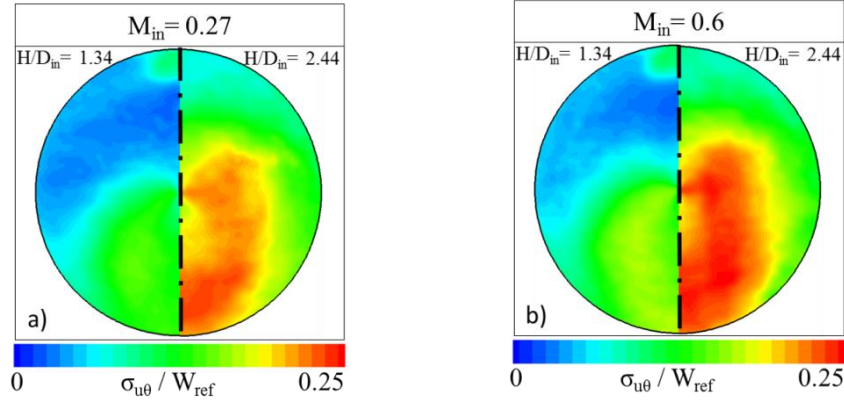


**Fig. 9** Non-dimensional circumferential velocity fluctuations  $\sigma_{u\theta}/W_{ref}$  at the AIP. (a-left):  $H/D_{in} = 1.34$ ,  $M_{in} = 0.27$ ,  $H/D_{in} = 2.44$ , (a-right):  $M_{in} = 0.27$ , (b-left):  $H/D_{in} = 1.34$ ,  $M_{in} = 0.6$ , (b-right):  $H/D_{in} = 2.44$ ,  $M_{in} = 0.6$ .

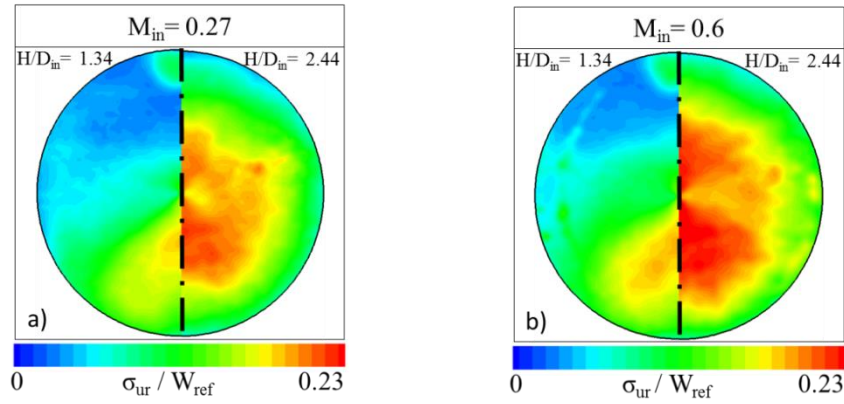


**Fig. 10** Non-dimensional radial velocity fluctuations  $\sigma_{ur}/W_{ref}$  at the AIP. (a-left):  $H/D_{in} = 1.34$ ,  $M_{in} = 0.27$ , (a-right):  $H/D_{in} = 2.44$ ,  $M_{in} = 0.27$ , (b-left):  $H/D_{in} = 1.34$ ,  $M_{in} = 0.6$ , (b-right):  $H/D_{in} = 2.44$ ,  $M_{in} = 0.6$ .

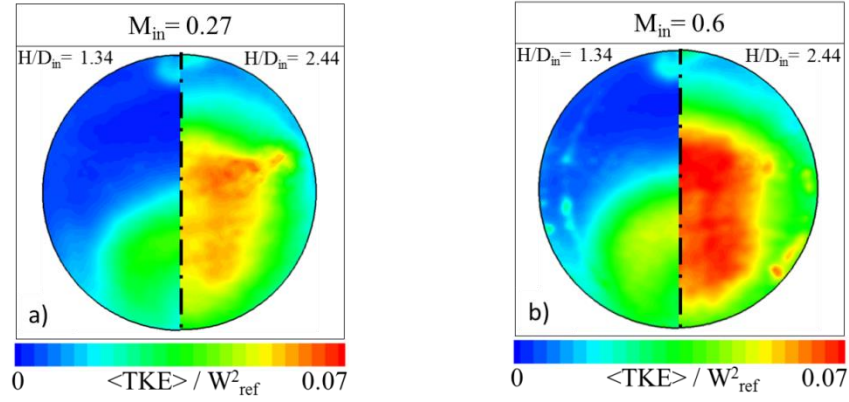


**Fig. 11 Non-dimensional time averaged turbulent kinetic energy distributions  $<TKE> / W_{ref}^2$  at the AIP. (a-**

**left):  $H/D_{in} = 1.34$ ,  $M_{in} = 0.27$ , (a-right):  $H/D_{in} = 2.44$ ,  $M_{in} = 0.27$ , (b-left):  $H/D_{in} = 1.34$ ,  $M_{in} = 0.6$ , (b-right):**

**$H/D_{in} = 2.44$ ,  $M_{in} = 0.6$ .**

The non-dimensional time averaged circumferential velocity at the AIP,  $<u_{\theta}> / W_{ref}$ , is shown in Fig. 8. Although there are differences between the two configurations and different Mach numbers, the distributions are generally similar. For the low offset S-duct with  $H/D_{in}=1.34$  the maximum circumferential velocity values are located at the lower part of the AIP with  $<u_{\theta}> / W_{ref} = 0.15$ . When  $M_{in}$  increases from 0.27 to 0.6, these regions increase in circumferential extent and the local maximum of  $<u_{\theta}> / W_{ref}$  increases slightly to 0.20. The AIP is positioned at the exit of the duct where it is still affected by the curvature of the duct and consequently there is a downward pitch of the flow that manifests as anti-symmetric regions of circumferential velocity. In addition, the classical secondary flows drive a strong circumferential velocity on either side of the centreline and close to the duct wall that is associated with the contra-rotating vortices. The general topology is similar for the high offset duct where the secondary flows are stronger and there is evidence of the associated local swirl distributions towards the centre of the duct. Relative to the low offset configuration, both the magnitude and extent of the swirl regions has increased and, as the duct has a higher offset, the downward pitching flow is also more prominent in the upper sections of the duct. Similarly, for the high offset duct,  $M_{in}$  has only a weak effect on the distribution of  $<u_{\theta}> / W_{ref}$ .

The unsteady non-dimensional circumferential and radial velocity fluctuations  $\sigma_{u\theta} / W_{ref}$  and  $\sigma_{ur} / W_{ref}$  (Fig. 9, Fig. 10) exhibit different characteristics in comparison with the  $\sigma_w / W_{ref}$  distributions (Fig. 7). For  $\sigma_{u\theta} / W_{ref}$  there are notable differences between the two configurations. At the low offset S-duct with  $H/D_{in}=1.34$  the maximum

circumferential velocity values are located at the lower part of the AIP where the levels are around 0.15. These increase to around 0.18 when  $M_{in}$  increases from 0.27 to 0.6 although the extent of the affected AIP region is broadly unaffected.. For this low offset configuration, the  $\sigma_{ur}/W_{ref}$  distributions (Fig. 10) similarly show the unsteadiness primarily associated with the lower part of the duct although the local maximum is now more centrally located in comparison with the  $\sigma_w/W_{ref}$  distribution. This is more similar to the  $\sigma_w/W_{ref}$  characteristic (Fig. 7). Overall, the indications are there are two main aspects that are affecting the flow unsteadiness. For these types of S-ducts, there is a flow separation that arises along the duct centerline and, in addition, there are the streamwise vortices that arise from the secondary flows<sup>26</sup>. Both of these mechanisms are unsteady and have an influence on the signatures of the unsteady velocities<sup>4,26</sup>. Although these aspects are interlinked, it is postulated that the shear layer associated with the centerline separation predominately affects the  $\sigma_w/W_{ref}$  distributions where the local maximum is positioned more towards the duct center and at the upper boundary of the main loss region. The distribution of  $\sigma_{ur}/W_{ref}$  is similarly positioned as  $\sigma_w/W_{ref}$  and is expected to be associated with the radial unsteadiness of the shear layer. In contrast, the peak levels of  $\sigma_{u\theta}/W_{ref}$  are located in a region more affected by the unsteadiness of the secondary flow vortices at the lower part of the AIP (Fig. 1b ,c). The local unsteadiness at the top of the duct is associated with a loss region that arises from the second bend of the duct. Although the flow is not expected to separate, there is a local loss that gives rise to the axial velocity deficit (Fig. 6) and the unsteadiness associated with it.

For the high offset S-duct with  $H/D_{in}=2.44$  the distributions of  $\sigma_{u\theta}/W_{ref}$  and  $\sigma_{ur}/W_{ref}$  are markedly different relative to the low offset configuration. The level of  $\sigma_{u\theta}/W_{ref}$  unsteadiness has increased to approximately 0.22 and a much greater portion of the region is affected across the central and lower parts of the duct (Fig. 9a).  $M_{in}$  has only a weak effect on the distribution of  $\sigma_{u\theta}/W_{ref}$  with a slight increase in peak values from 0.22 to 0.25. Relative to the low offset case ( $H/D_{in}=1.34$ ), the distribution of  $\sigma_{ur}/W_{ref}$  for the high offset configuration ( $H/D_{in}=2.44$ ) changes so that there is an increase in the levels of unsteadiness from about 0.15 to 0.22 and the distribution is dominated by a more central location and a substantially greater extent. For the  $H/D_{in}=2.44$  configuration, the increased offset of the duct has an impact on both the centerline separation as well as the secondary flows. The flow separates further upstream and the separated shear layer takes a more central position<sup>8</sup>. This results in a distorted flow at the duct exit, parts of which demonstrate a vertical oscillation around the AIP center that manifest as high unsteadiness of the radial velocity in the high offset S-duct. In addition, the increased offset produces a stronger secondary flow that by the

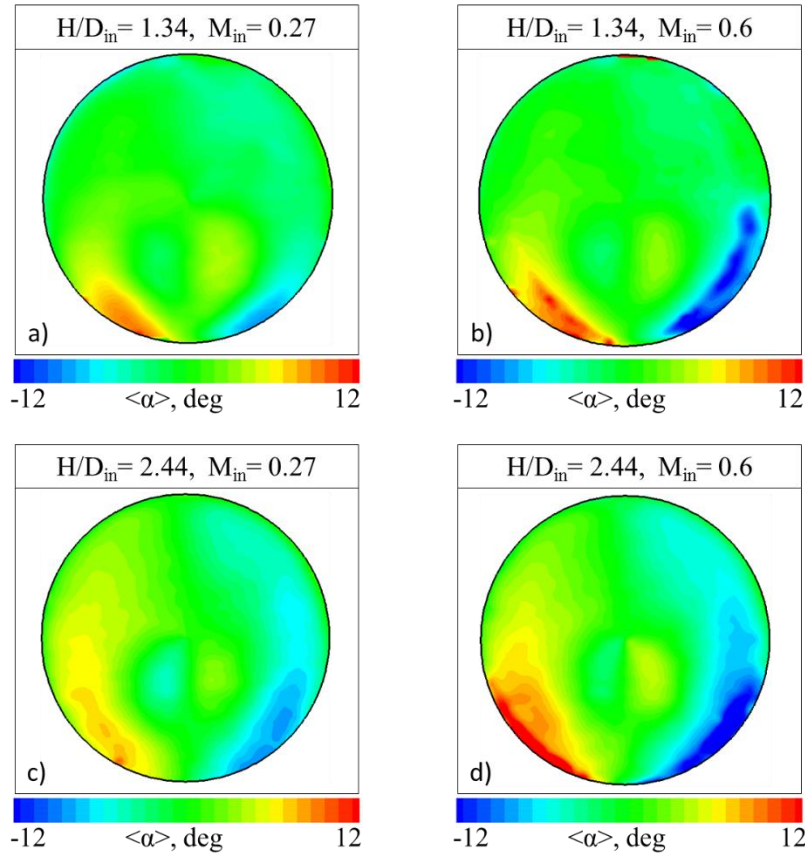
exit of the duct has also migrated to a more central position<sup>26</sup>. Consequently, both the  $\sigma_{u\theta}/W_{ref}$  and  $\sigma_{ur}/W_{ref}$  distributions for the  $H/D_{in}=2.44$  duct are also more centrally positioned with an increased extent. This is in agreement with unsteady total pressure characteristics from computational studies which analyzed similar geometries<sup>8,26</sup>. A measure of the relative importance of the individual terms and of the overall unsteadiness is the time-averaged non-dimensional turbulent kinetic energy ( $\langle TKE^* \rangle = \langle \frac{1}{2} [u_r'^2 + u_\theta'^2 + w'^2] / W_{ref}^2 \rangle$ ). For the low offset configuration at both Mach numbers the  $\langle TKE^* \rangle$  is dominated in the lower part of the duct with the local maximum associated with the  $\sigma_w/W_{ref}$  terms (Fig. 11). For the high offset case with  $H/D_{in}=2.44$  the relatively high values of  $\langle TKE^* \rangle$  levels are approximately 50% greater and the peak levels arise at the center of the AIP. When  $M_{in}$  is increased from 0.27 to 0.60, the peak values increase by about 20% and the extent of the region slightly increases.

The swirl angle  $\alpha$  is defined by the angle between the circumferential velocity  $u_\theta$  and the axial velocity  $w$ <sup>7</sup>. The time averaged swirl angle distributions are shown in Fig. 12 for both configurations as well as for Mach 0.27 and 0.60. Some notable differences can be observed between the two cases. The high swirl regions with values close to  $\pm 8^\circ$ , are more localized in the low offset configuration and mostly restricted within the lower part of the AIP (Fig. 12a, b). The values across the rest of the AIP remain in the range of  $\pm 4^\circ$ . Clearly, the distributions of  $\alpha$  are primarily related to the circumferential velocity (Fig. 8) which is driven by the pitching of the flow and the development of the secondary flow vortices at the lower part of the AIP (Fig. 1). For the high offset configuration the peak swirl angles are approximately  $\pm 10^\circ$  and the extent of the affected region has increased relative to the low offset configuration (Fig. 12 a,b). When  $M_{in}$  increases from 0.27 to 0.6 only a modest effect in the swirl angle distributions is observed for both configurations with an increase in levels to approximately  $\pm 12^\circ$ . The distributions of the unsteady swirl angle,  $\sigma_\alpha$ , are shown in Fig. 13 and for both cases it is significant that the local  $\sigma_\alpha$  levels are over  $13^\circ$  which is, in general, greater than the time averaged levels. Duct 1 ( $H/D_{in}=1.34$ ) shows a more localized unsteady swirl angle region located at the lower part of the AIP (Fig. 13). The high offset configuration shows a much larger region of unsteady swirl angles and in this case it also encompasses the regions of high unsteadiness of the out-of-plane velocity in the center (Fig. 7) as well as circumferential velocity (Fig. 9) which extends from the lower part to the center. Inlet Mach number has only a small effect on the swirl unsteadiness where the peak values increase from  $13^\circ$  to about  $15^\circ$ . and the distribution remains broadly unchanged. These levels of spatial variation in time averaged swirl angle, and the additional very high unsteady variations in inlet swirl angle, pose a significant design challenge from the perspective of the impact on a downstream axial compression system.

1        The time averaged and simple statistical assessment of the flow unsteadiness does not reveal the complexity of  
2 the flow and to illustrate this, some sample snapshots of the distributions of the out-of-plane velocity and swirl angle  
3 are shown in Fig. 14 for Duct 2 at inlet Mach = 0.27. It is of worth noting the substantial variations of the flow in  
4 each snapshot compared to the time averaged distribution. Although this simply illustrates the substantial variations  
5 in the flow field, it begins to highlight the difficulties encountered by a conventional 40-probe rake in sufficiently  
6 measuring the flow distortion. This is further compounded by the unsteady variations in swirl angle that  
7 conventionally is measured with even fewer probes and usually only in a time averaged sense. Overall, the very  
8 substantial changes in swirl angle and flow topology highlight that AIP assessments based on a typical 40 probe  
9 pressure rake may be insufficient to capture the complex nature of the flow.

10

1

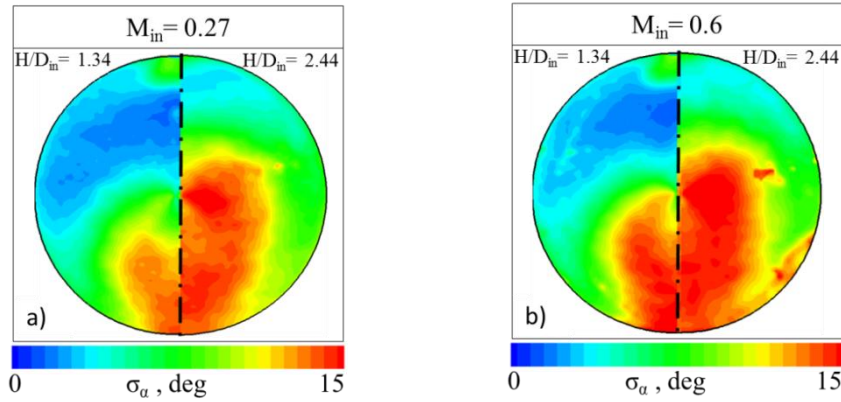


2

3

**Fig. 12** Time averaged swirl angle distributions  $\langle \alpha \rangle$  at the AIP. (a):  $H/D_{in} = 1.34$ ,  $M_{in} = 0.27$ , (b):  $H/D_{in} = 1.34$ ,  $M_{in} = 0.6$ , (c):  $H/D_{in} = 2.44$ ,  $M_{in} = 0.27$ , (d):  $H/D_{in} = 2.44$ ,  $M_{in} = 0.6$ .

4



5

6

**Fig. 13** Swirl angle fluctuations  $\sigma_u$  at the AIP. (a-left):  $H/D_{in} = 1.34$ ,  $M_{in} = 0.27$ , (a-right):  $H/D_{in} = 2.44$ ,  $M_{in} = 0.27$ , (b-left):  $H/D_{in} = 1.34$ ,  $M_{in} = 0.6$ , (b-right):  $H/D_{in} = 2.44$ ,  $M_{in} = 0.6$ .

7

8

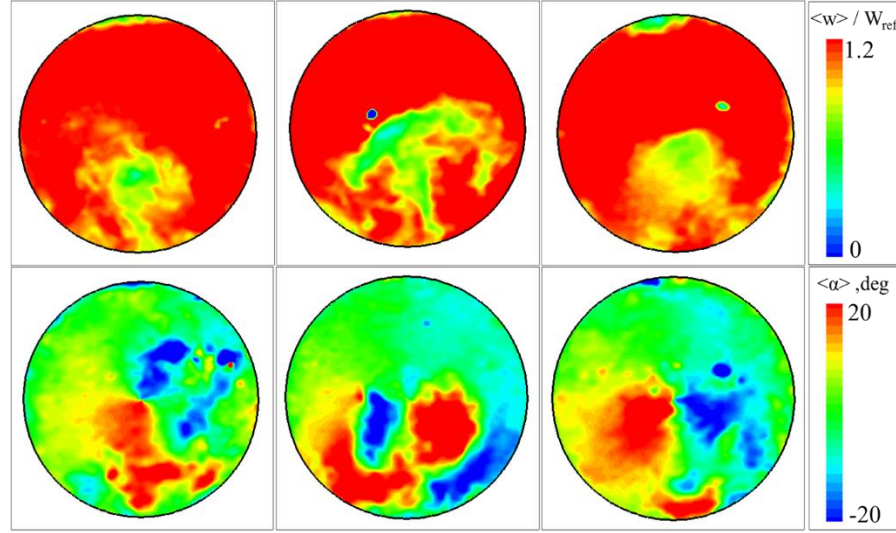


**Fig. 14** (top): Non-dimensional instantaneous axial velocity distributions  $\langle w \rangle / W_{ref}$  and (bottom): instantaneous swirl angle distributions  $\alpha$  at the AIP for the high offset S-duct ( $H/D_{in}=2.44$ ) at  $M_{in} = 0.27$ .

## B. Flow Distortion Assessment

As part of the industry convention on engine inlet flow distortion a range of flow distortion descriptors are proposed for swirl related distortion. For the assessment of swirl distortion a swirl coefficient based on the most distorted  $60^\circ$  sector,  $SC(60)$ , is used<sup>27,28</sup> and is defined as:

$$SC(60) = \frac{\max(u_\theta[60])}{W_{ref}} \quad (4)$$

where  $\max(u_\theta[60])$  is the mean value of circumferential velocity in the  $60^\circ$  sector with the highest  $u_\theta$  average and  $W_{ref} = \frac{1}{A} \int_A \langle w(r, \theta, t) \rangle dA$  is the area averaged axial velocity at the AIP. In addition, standards have been introduced to define a set of swirl descriptors by categorizing the types of swirl distortion into four groups; bulk swirl, tightly-wound vortices, paired swirl and cross flow swirl<sup>7</sup>. The definition and interpretations of these is based on a “ring and rake” approach as shown in Fig. 15, which is a typical experimental approach for AIP distortion measurements. The one-per-revolution, paired swirl pattern is shown in Fig. 16 and serves to illustrate the definitions of the swirl distortion descriptors<sup>7</sup>.

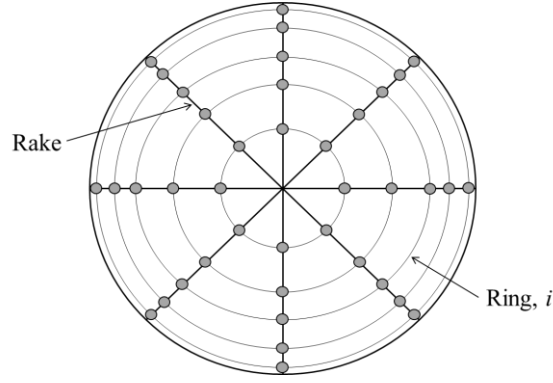


**Fig. 15 8x5 ring and rake AIP discretization for inlet flow distortion measurements<sup>15</sup>.**

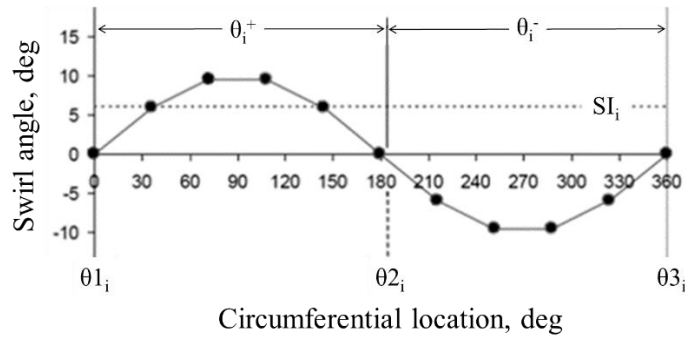


**Fig. 16 Typical one-per-rev symmetric paired swirl pattern for single immersion<sup>7</sup>.**

Theta plus,  $\theta_i^+$ , is the circumferential extent of the positive (co-rotating) swirl region and theta minus,  $\theta_i^-$ , is the circumferential extent of the negative (counter-rotating) swirl region. The extents of these regions are defined when the swirl angle changes sign. As shown in Fig. 16, the  $\theta^+$  extent is:

$$\theta_i^+ = \theta_{2_i} - \theta_{1_i} \quad (5)$$

and  $\theta^-$  extent is

$$\theta_i^- = \theta_{3_i} - \theta_{2_i} \quad (6)$$

Based on these definitions the distortion descriptors are extended to characterize swirl of multiple-per-rev patterns measured on a given circumferential  $i$ -th ring. The swirl descriptors are defined using index  $i$  to identify the circumferential ring and index  $k$  to identify the various swirl pairs along ring  $i$ . Sector swirl (SS) quantifies the azimuthally averaged positive,  $SS_{i,k}^+$ , and negative,  $SS_{i,k}^-$ , swirl content at a given radial ring.

$$SS_{i,k}^+ = \frac{1}{\theta_{i,k}^+} \int_{\theta_{i,k}^+} \alpha(\theta)_{i,k} d\theta \quad (7)$$



$$SS_{i,k}^- = \frac{1}{\theta_{i,k}^-} \int_{\theta_{i,k}^-} \alpha(\theta)_{i,k} d\theta \quad (8)$$

Swirl intensity (SI) represents the average of the absolute swirl angle in degrees for a considered ring  $i$ . The average swirl intensity along a ring  $i$  is given by the following expression where  $m$  is the total number of swirl pairs from  $k=1$  to  $k=m$ .

$$SI(i) = \frac{\sum_{k=1}^m SS_{i,k}^+ \cdot \theta_{i,k}^+ + \sum_{k=1}^m |SS_{i,k}^-| \cdot \theta_{i,k}^-}{360} \quad (9)$$

Swirl directivity (SD) represents the overall rotational direction of the swirl with respect to the compressor rotation at each ring  $i$ . In other words, this parameter provides the equivalent bulk swirl rotational direction along a ring  $i$  as shown graphically in Fig. 17. It is defined as:

$$SD(i) = \frac{\sum_{k=1}^m SS_{i,k}^+ \cdot \theta_{i,k}^+ + \sum_{k=1}^m SS_{i,k}^- \cdot \theta_{i,k}^-}{\sum_{k=1}^m SS_{i,k}^+ \cdot \theta_{i,k}^+ + \sum_{k=1}^m |SS_{i,k}^-| \cdot \theta_{i,k}^-} \quad (10)$$

The Swirl Pairs (SP) parameter indicates the number of pairs of positive and negative swirl regions present along a ring  $i$ . The spectrum of swirl pairs is graphically shown in Fig. 18 and the descriptor is defined as:

$$SP(i) = \frac{\sum_{k=1}^m SS_{i,k}^+ \cdot \theta_{i,k}^+ + \sum_{k=1}^m |SS_{i,k}^-| \cdot \theta_{i,k}^-}{2 \cdot \text{Max}\{SS_{i,k}^+ \cdot \theta_{i,k}^+, |SS_{i,k}^-| \cdot \theta_{i,k}^-\}}_{k=1, \dots, m} \quad (11)$$

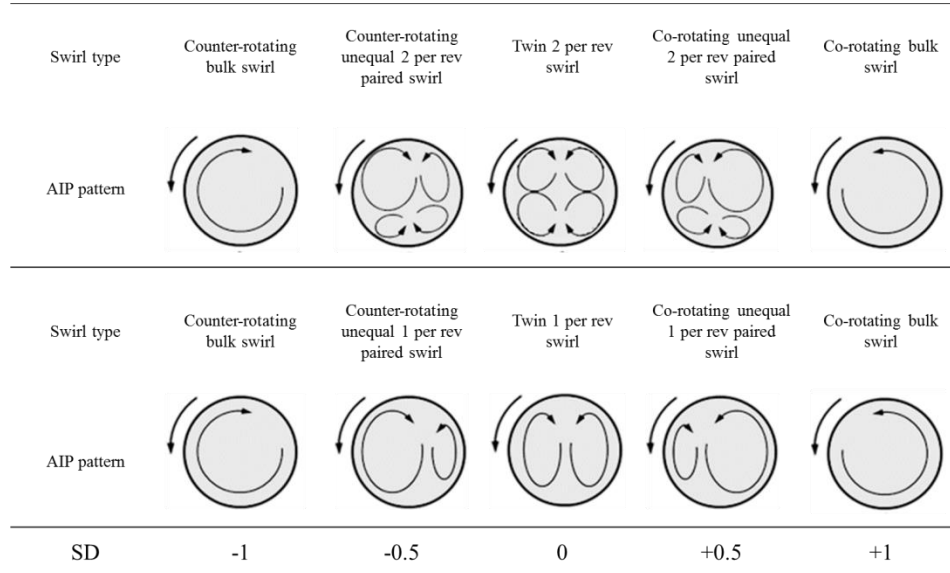


**Fig. 17 Swirl directivity for multiple per-rev swirl distortion compared to a one per-rev spectrum<sup>7</sup>.**

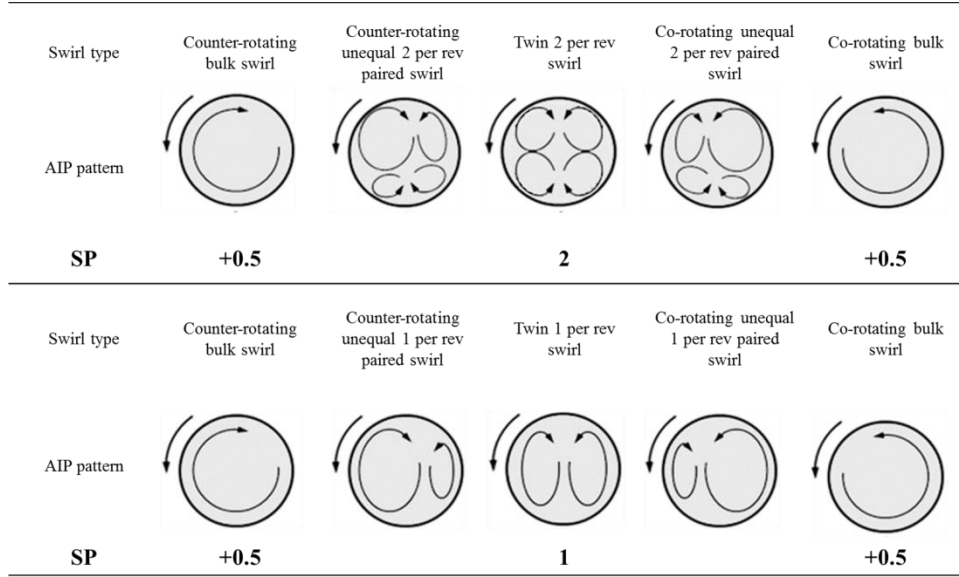


**Fig. 18 Swirl pairs spectrum for multiple per-rev swirl distortion compared to a one per-rev spectrum<sup>7</sup>.**

For the calculation of the statistical properties of the descriptors, a value was obtained for each instantaneous flow snapshot based on a resolution of a typical 8x5 rake. For the calculation of a single swirl descriptor value for each instantaneous snapshot at a given  $M_{in}$  from the 8x5 resolution data an area weighted average approach was used. The time averaged values were calculated based on the individual descriptors determined for each of the 1000 snapshots for each configuration. The reason that the spatial resolution of the PIV was under-sampled for the calculation of the descriptors is that the industry standard and evaluation of the parameters is based on the low resolution and it was decided to be consistent with this approach and knowledge base and to simulate the spatial characteristics of a conventional measurement approach.

The time average and standard deviation of the swirl descriptors are presented in Table 2 and Fig. 19. As expected, based on the distributions and variations in swirl angle (Fig. 12, Fig. 13), the swirl distortion of the high offset configuration is greater than that of the low offset. Across the range of  $M_{in}$  the time averaged swirl intensity ( $SI_{mean}$ ) is around 1.8 times higher for the high offset configuration and there is a broadly similar increase in the unsteady variation in  $SI_{std}$ . The effect on  $SI_{std}$  is slightly less with an average increase of about 1.5 relative to the  $H/D_{in}=1.34$  configuration. Although the relative increases are very slightly less, the same characteristics are observed in the SC60 average and unsteady metrics. A key consideration is the unsteady variation in the swirl distortion metrics as previous data has only focused on the average levels. The current measurements show that there are substantial unsteady aspects where for the  $H/D_{in}=1.34$  configuration the  $SI_{max}$  and  $SC60_{max}$  are 1.9 and 1.7

times greater than the average levels, respectively. Similarly for the  $H/D_{in}=2.44$  configuration the  $SI_{max}$  and  $SC60_{max}$  are 1.7 and 1.5 times greater than the average levels, respectively. This highlights some of the limitations of a conventional time averaged measurement and the potential underestimation of the swirl distortion.

The distortion metric of swirl directivity (SD) is limited to a range of  $\pm 1$ , with a value of 0 representative of a symmetric flow field (Fig. 17), for which the SP minima are  $\pm 0.5$  with a maximum value related to a symmetric flow containing multiples of vortex pairs (Fig. 18). For both the high- and low-offset configurations, the time-averaged swirl directivity (SD) is approximately zero (Table 2) which indicates a symmetry of the average swirl distortion pattern with respect to the vertical axis (Fig. 17). This is relatively insensitive to the Mach number. The  $SP_{mean}$  is broadly around 1.0 that indicates that, on average, a twin one-per-rev swirl distortion pattern is present in both cases. However, there are notable variations and the maximum SP value for the low offset configuration is almost 2 which indicates that at some occasions the flow field comprise 2 pairs of contra-rotating swirl regions. It is also of note that, in spite of the increased curvature for the high offset configuration, the maximum SP is approximately 1.5 and therefore not so clearly related to a double swirl pair topology. The  $SD_{std}$  for the high offset case is also about 1.8 times greater than the low offset configuration although both cases are similarly limited by  $SD_{max}$  of about 1.0. Overall, it quantifies the impact of the duct offset on the flow distortion characteristics primarily due to the changes in the centerline separation and the secondary flows.

**Table 2 Area-averaged swirl descriptor statistical properties.**

	$H/D_{in}=1.34$ $M_{in}=0.27$	$H/D_{in}=1.34$ $M_{in}=0.45$	$H/D_{in}=1.34$ $M_{in}=0.60$	$H/D_{in}=2.44$ $M_{in}=0.27$	$H/D_{in}=2.44$ $M_{in}=0.45$	$H/D_{in}=2.44$ $M_{in}=0.60$
$SI_{mean}$ ( $^{\circ}$ )	4.8	5.3	5.5	8.5	9.2	9.8
$SI_{std}$ ( $^{\circ}$ )	0.9	1	1.1	1.6	1.7	1.7
$SI_{max}$ ( $^{\circ}$ )	8.9	10.2	10.7	14.9	15.2	15.6
$SC60_{mean}$	0.13	0.14	0.17	0.24	0.25	0.26
$SC60_{std}$	0.03	0.03	0.03	0.04	0.05	0.05
$SC60_{max}$	0.22	0.26	0.27	0.37	0.39	0.37
$SD_{mean}$	-0.11	-0.09	-0.1	0	0.02	-0.02
$SD_{std}$	0.23	0.23	0.25	0.43	0.42	0.4
$SD_{max}$	0.84	0.86	0.95	0.95	0.92	0.92
$SP_{mean}$	1.16	1.15	1.15	0.9	0.88	0.9
$SP_{std}$	0.17	0.17	0.17	0.14	0.14	0.13
$SP_{max}$	1.65	1.86	1.96	1.47	1.52	1.43

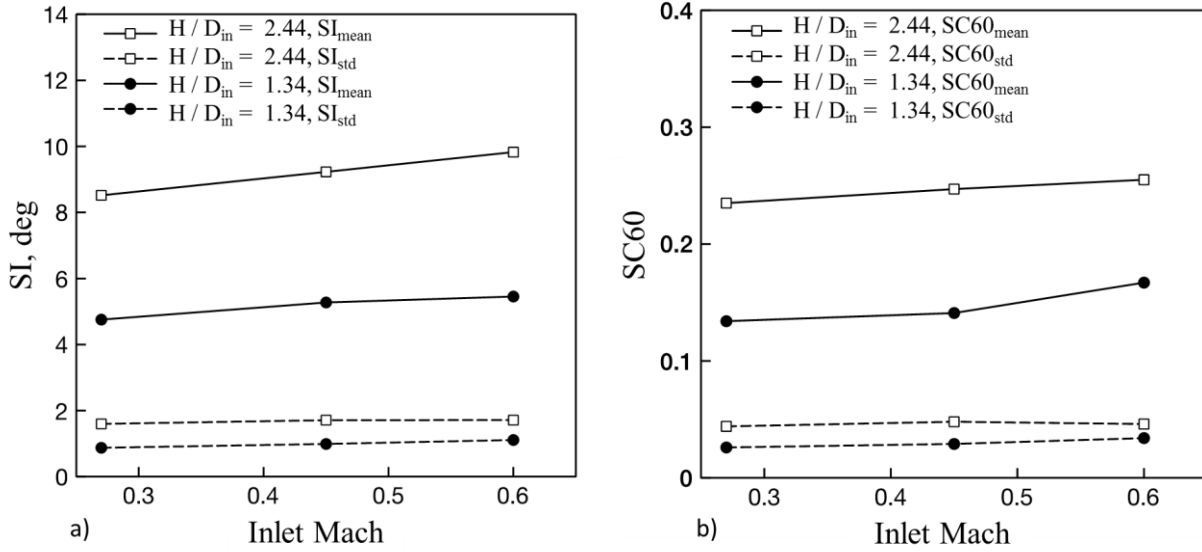


**Fig. 19 SI (a) and SC60 (b) characteristics for the low and high offset S-duct across the range of  $M_{in}$ .**

In addition to the mean and the variance of SI, SD, SP and SC60 the skewness and the kurtosis of the unsteady metrics were also determined. The interest is in understanding the characteristics of the unsteady variations that arise in the flow field. In particular, from the perspective of a compressor designer, it is important to not just consider the mean and standard deviation, but also the likelihood of adverse distortion events. This is because of the highly dynamic nature of the flow and the potential sensitivity of the engine to individual events which have a global impact on the engine operation. The first step in this process, with particular emphasis on the previously neglected swirl aspects, is the evaluation of the skewness and kurtosis of the swirl descriptors. Skewness measures the symmetry of a distribution with respect to the Gaussian distribution and kurtosis quantifies whether the shape of data distribution matches the Gaussian distribution<sup>29</sup>. A Gaussian distribution has a skewness of 0.0 and a kurtosis index of 3.0. A flatter, platykurtic, distribution obtains kurtosis values lower than 3 while a more peaked, leptokurtic, distribution has kurtosis higher than 3. The skewness of the swirl descriptors, SI, SD, SP, SC60, showed a deviation of their distribution from the Gaussian characteristic towards the positive direction i.e. towards the right side of the mean. Although the skewness is at a medium level in the range of 0 to 0.6<sup>22</sup>, it is of particular note that for the particular SI and SC60 parameters the skewness remained positive with values in the range of 0.4 to 0.6. This highlights a greater likelihood of the occurrence of adverse swirl distortion events. This characteristic was common between the two S-ducts tested across the entire range of inlet Mach numbers. All swirl descriptors demonstrated a

kurtosis level that was within  $\pm 15\%$  of the normal distribution kurtosis value of 3.0. Inlet Mach number had very little effect on kurtosis<sup>22</sup>.

Although the standard deviation along with the skewness and kurtosis metrics provide a quantitative description of the statistical characteristics of the distortion metrics, it is useful to consider the relationship between the metrics as evaluated for each snapshot (Fig. 20). This type of analysis of the unsteady swirl distortion parameters has not been possible previously and is one of the key advantages of the S-PIV approach presented here due to the combinations of spatial resolution and synchronous acquisition. The relationship between the SC60 and SI descriptors for the two configurations is shown in Fig. 20 in the form of distortion maps. These scatter plots illustrate the distortion metrics of the entire population of flow snapshots acquired by the S-PIV measurements. The low offset configuration at  $M_{in} = 0.27$ , demonstrates an SI range between  $2^\circ$ - $9^\circ$  while for the high offset configuration at  $M_{in} = 0.27$  the SI range is approximately  $5^\circ$ - $15^\circ$ . In terms of SC60, the low offset case at  $M_{in} = 0.27$  demonstrates a range between 0.03-0.22 that increases to 0.05-0.37 for the high offset geometry. The inlet Mach number has a modest impact on the range of SC60 and SI for both configurations (Fig. 20b). The cloud plots quantify the very substantial differences between the mean distortion parameter values and the variation of distortion events. This again highlights the notable drawbacks of a conventional distortion measurement approach that does not capture these events and the richness of the data that is obtained using the S-PIV method. Of particular interest are the differences between the mean values and the peak distortion events that may have the most significant impact on the compression system.

The distortion metrics of SP and SD are also of interest in the evaluation of the S-duct distortion metrics. For both S-ducts and both Mach numbers (Fig. 21), the mean values are  $SD \approx 0$  and  $SP \approx 1$  where it is recalled that this signifies a single pair of vortices with equivalent size (Fig. 17 and Fig. 18). However, there are notable excursions from this topology that have significant effects on the distortion levels. Although there is the expected scatter in the data due to the highly unsteady and complex nature of the flow, there is an indicated relationship whereby as SP reduces from peak values in the region of 1.5-2.0 towards 0.5 there is a concomitant deviation of SD from 0 to  $\pm 1$  (Fig. 21). This signifies that at these moments the swirl structure is not symmetric but is more akin to a single biased swirling flow rotating in either clock- or anti-clock wise direction (Fig. 17, Fig. 18). This indicates that there is a mechanism whereby the nominal symmetric flow is modulated to the asymmetric condition that switches orientation from positive to negative swirl directions. At  $M_{in} = 0.27$  this characteristic is common for both the high- and low-

offset configurations. At  $M_{in} = 0.60$  although the same general characteristics are exhibited there is a notable increase in the SP levels for the low-offset duct to a maximum  $SP \approx 2$  for  $SD=0$ . This is indicative of a change in the flow field topology from a conventional single swirl pair to a set of two contra-rotating swirl pairs at the AIP (Fig. 21). Moreover, during these swirl switching events, where the flow is biased towards one side, the SI index generally obtains a maximum value for both configurations (Fig. 22 and Fig. 23). This supports the observation that the more extreme swirl distortion events are associated with the vortex switching and the single-sided biased swirl patterns. Overall, from the assessment of the individual snapshots of the swirl distortion metrics it is clear that the dynamic nature of the flow gives rise to substantial variations in the descriptors. Nearly all previous work has evaluated swirl distortion from a time-averaged view and the results here clearly show that the flow field is substantially different from the time averaged descriptors. The significance of this difference is further heightened by the evidence whereby the variations from the time-averaged data are associated with a more potent distorted flow field and therefore shows how previous assessments have been based on overly benign evaluations. Consequently, this has potentially significantly underestimated the level of swirl distortion introduced by complex intakes and the likely impact on the stability of the compression system.

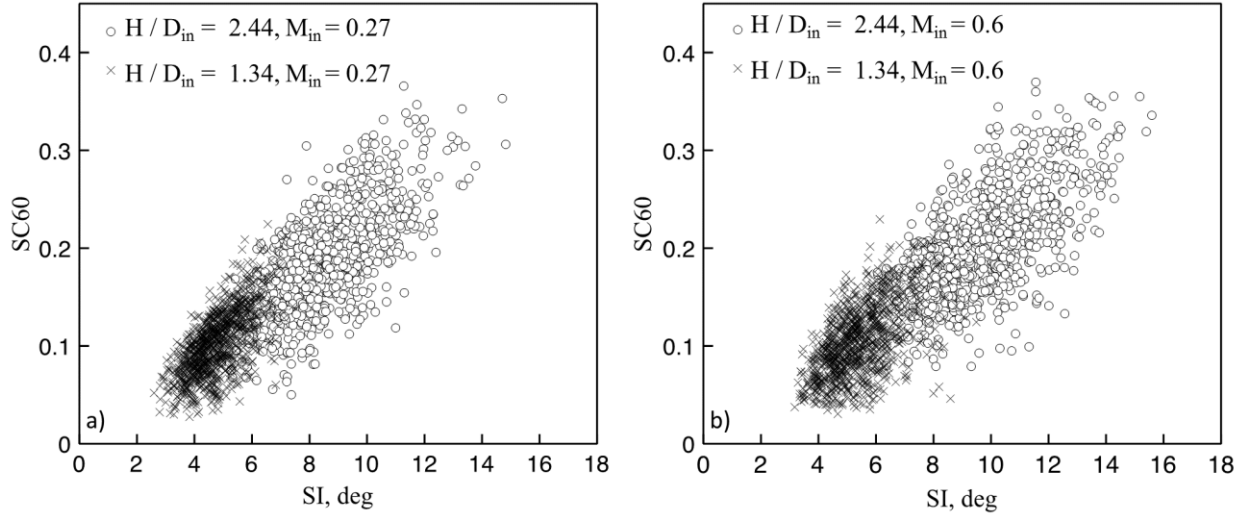


**Fig. 20 SC60-SI cloud plots for the  $H/D_{in} = 1.34$  and  $H/D_{in} = 2.44$  configurations (a):  $M_{in} = 0.27$ , (b):  $M_{in} = 0.6$ .**

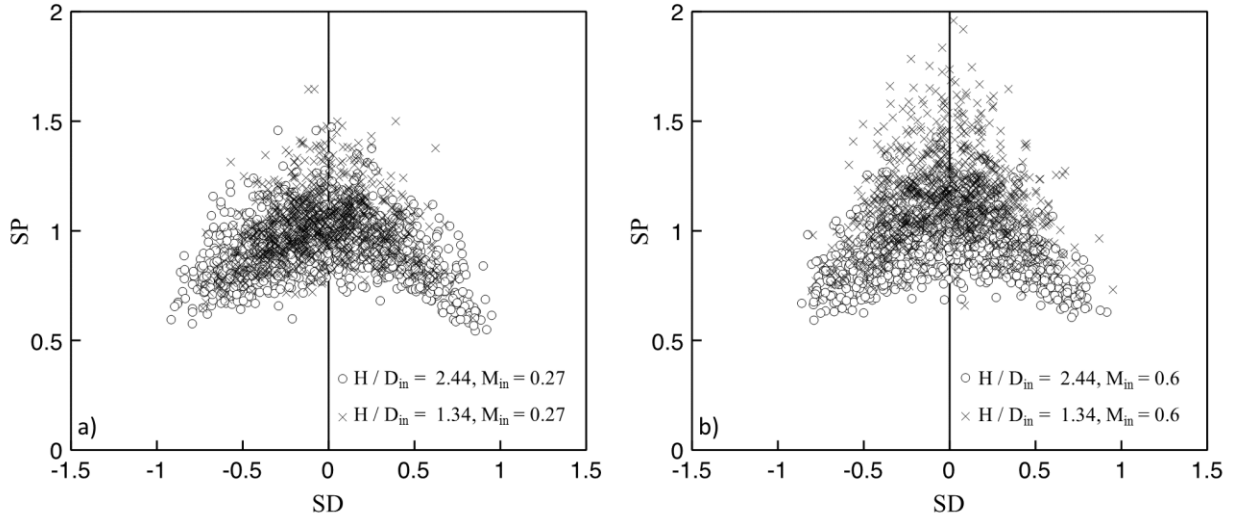


**Fig. 21 SP-SD distortion cloud plots for the  $H/D_{in} = 1.34$  and  $H/D_{in} = 2.44$  configuration. (a):  $M_{in} = 0.27$ , (b):  $M_{in} = 0.6$ .**

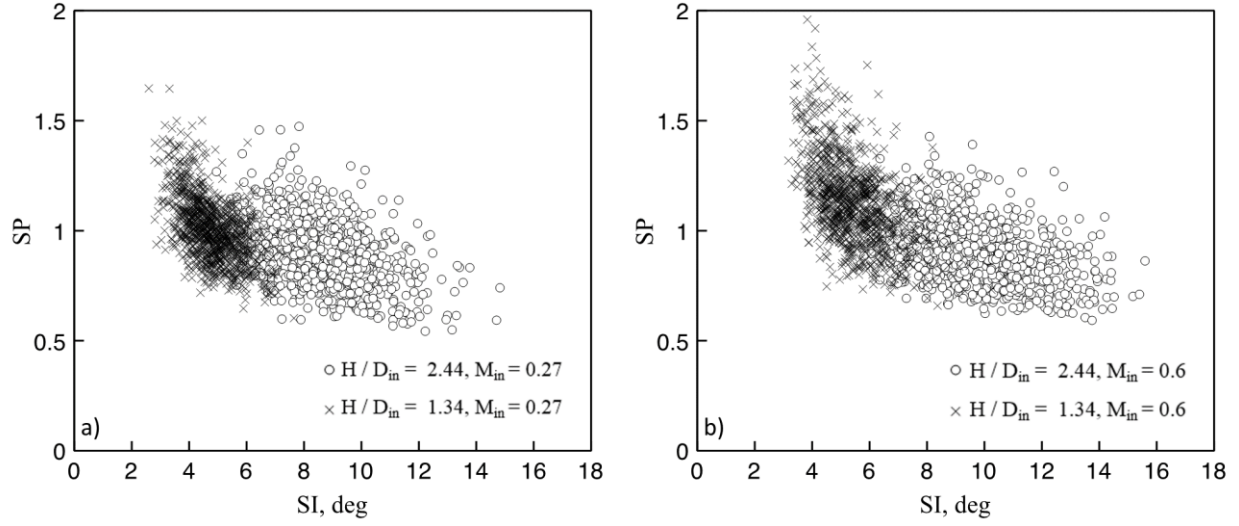


**Fig. 22 SP-SI distortion cloud plots for the  $H/D_{in} = 1.34$  and  $H/D_{in} = 2.44$  configuration. (a):  $M_{in} = 0.27$ , (b):  $M_{in} = 0.6$ .**

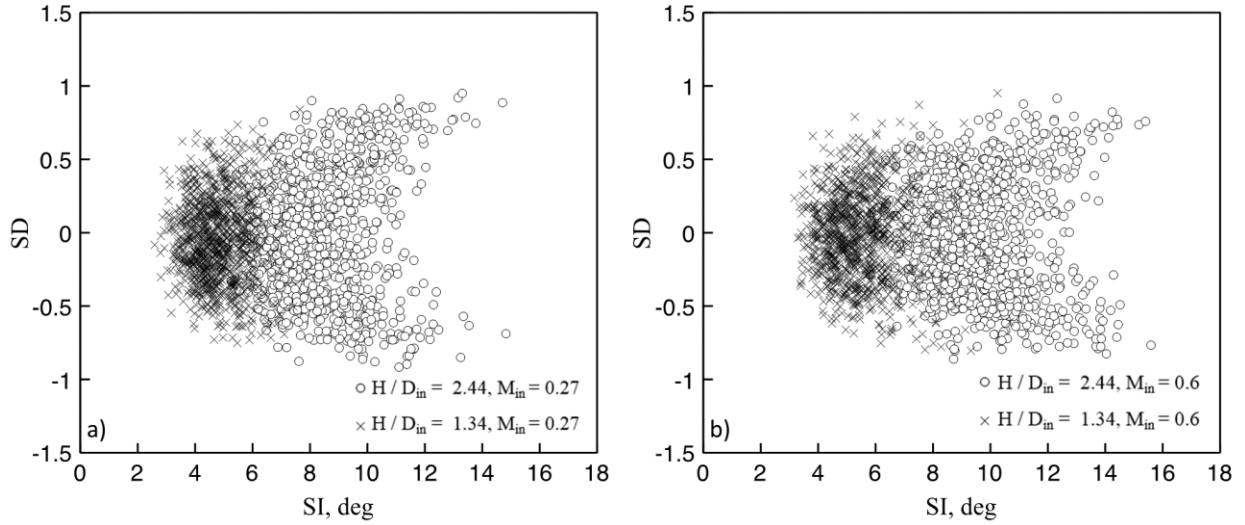


**Fig. 23 SD-SI distortion cloud plots for the  $H/D_{in} = 1.34$  and  $H/D_{in} = 2.44$  configuration. (a):  $M_{in} = 0.27$ , (b):  $M_{in} = 0.6$ .**

#### IV. Conclusions

Flow distortion assessments based on conventional pressure probe methods are typically severely limited by the viable spatial resolution. The unsteady nature of the distorted flow at the duct exit also means that synchronous data is required to quantify the dynamic aspects of the distortion. S-PIV enables the acquisition of such synchronous data,



with the additional benefit of a much higher spatial resolution compared to conventional probe-based techniques. This investigation reports on the novel use of S-PIV to measure the full-face distorted flow field at the exit of S-duct configurations and to provide an evaluation of swirl distortion descriptors based on these high-resolution synchronous measurements. The main challenges associated with the application of S-PIV for the measurement of the velocity fields in confined flows are addressed. The acquired velocity fields feature approximately 9,000 vectors across the entire AIP that corresponds to a resolution of 0.8% of the AIP diameter. This is significantly higher than the standard rake measurements that typically feature 40 measurement points across the AIP. The S-PIV technique enabled flow analysis in terms of snapshot, statistical and time averaged measurements for two S-duct configurations with offset to inlet diameter ratios of  $H/D_{in}$  1.34 and 2.44 respectively across a range of inlet Mach numbers between 0.27-0.6. The comparisons of the AIP flow fields revealed that the high offset configuration generates a more distorted as well as a more unsteady flow. The regions of high swirl angle unsteadiness are not uniquely co-located with the highly unsteady out-of-plane velocity part of the flow, and it is postulated that these elements are related to different features of the distorted flow. Inlet Mach number has only a modest effect on both the steady and unsteady characteristics.

The conventional swirl distortion descriptors for swirl intensity (SI), directivity (SD), swirl pairs (SP), and SC60 were calculated across the range of inlet Mach numbers. As expected, the high offset duct of  $H/D_{in} = 2.44$  demonstrates more distorted flows which in terms of average SI and SC60 are about 80% greater than those of the low offset case ( $H/D_{in} = 1.34$ ). Similar relative changes in the unsteady levels of SI and SC60 are measured between the high- and low offset configurations. The swirl descriptors show weak dependency upon the inlet Mach number for both S-ducts. The statistical analysis of the swirl properties showed that the kurtosis is similar to that of a Gaussian distribution, but that there is a positive skewness in the SI and SC60 parameters with a bias towards the more adverse distortion conditions. Distortion cloud maps show that the flow is highly unsteady with a characteristic switching of the distortion that also leads to higher distortion levels. Overall, the results show that the conventional assessment of swirl distortion based on time-averaged assessments substantially underestimates the distortion level and that the rarer distortion events give rise to more potent threats to the compression system.

Overall, the capability of S-PIV for a highly distorted, complex flow field was demonstrated whereby the substantially rich spatial resolution that S-PIV provided is used to better understand the unsteady swirl distortion of such flow fields. The demonstrated synchronous spatial resolution is approximately 250 times greater than that

provided by a typical conventional system. The key capability of the method to acquire full planar field synchronous data enables an of the velocity field and swirl distortion metrics at a spatial resolution that has not been previously possible. This is a key step forward in unlocking the complex aerodynamics that dominate advanced intake–engine systems.

## References

<sup>1</sup> Kawai, R., Friedman, D., Serrano, L., “Blended Wing Body Boundary Layer Ingestion Inlet Configuration and System Studies”, NASA Contract Report CR-2006-214534, 2006.

<sup>2</sup> Gohardani, A., S., “A Synergistic Glance at the Prospects of Distributed Propulsion Technology and the Electric Aircraft Concept for Future Unmanned Air Vehicles and Commercial/Military Aviation”, *Progress in Aerospace Sciences*, Vol. 57, 2013, pp. 25-70.

<sup>3</sup> Wellborn, S. R., Reichert, B. A., and Okiishi, T. H., “Study of the Compressible Flow in a Diffusing S-Duct”, *AIAA Journal of Propulsion and Power*, Vol. 10, No. 5, 1994, pp. 668–675.

DOI: 10.2514/3.23778

<sup>4</sup> Delot, A.-L., Garnier, E., Pagan, D., “Flow Control in a High-Offset Subsonic Air Intake”, *47<sup>th</sup> AIAA/ASME/SAE/ASEE Joint Propulsion Conference and Exhibit*, AIAA 2011-5569, San Diego, California, USA, 2011.

DOI: 10.2514/6.2011-5569

<sup>5</sup> Garnier, E., Leplat, M., Monnier, J., C., Delva, J., “Flow Control by Pulsed Jet in a Highly Bended S-Duct”, *6<sup>th</sup> AIAA Flow Control Conference*, AIAA 2012-3250, New Orleans, Louisiana, USA, 2012.

DOI: 10.2514/6.2012-3250

<sup>6</sup> Garnier, E., “Flow Control by Pulsed Jets in a Curved S-Duct: A Spectral Analysis”, *AIAA Journal*, Vol. 53, No. 10, 2015, pp. 2813-2827.

DOI: 10.2514/1.J053422

<sup>7</sup> “A Methodology for Assessing Inlet Swirl Distortion”, Aerospace Information Report 5686, Society of Automotive Engineers, Warrendale, PA, 2007.

<sup>8</sup> Chiereghin, N., MacManus, D., Savill, M., Dupuis, R., “Dynamic Distortion Simulations for Curved Aeronautical Intakes”, *Advanced Aero Concepts, Design and Operation*, Bristol, UK, 2014.

<sup>9</sup> “Inlet Total Pressure Distortion Considerations for Gas Turbine Engines”, Society of Automotive Engineers, Aerospace Information Report 1419, Rev. A, Warrendale, PA, 1999.

<sup>10</sup>Cousins, W., T., “History, Philosophy, Physics and Future Directions of Aircraft Propulsion System / Inlet Integration”, *Proceedings of ASME Turbo Expo 2004*, GT2004-54210, Vienna, Austria, 2004.

<sup>11</sup>Anderson, B., H., Baust, H., D., Agrell, J., “Management of Total Pressure Recovery, Distortion and High Cycle Fatigue in Compact Air Vehicle Inlets”, NASA, TM 2002-212000, 2002.

<sup>12</sup>Moore, M., T., “Distortion Data Analysis”, National Technical Information Service, General Electric Company, AFAPL-R-72-111, 1972.

<sup>13</sup>Samuelsson, I., “Test of an UCAV Air Inlet Duct (Eikon) at Static Conditions in FOI Suckdown Facility”, FOI, FOI-R-1572-SE, 2005.

<sup>14</sup>Johansson, M., “FoT25 2003-2005 Propulsion Integration Final Report”, FOI, FOI-R-2017-SE, 2006.

<sup>15</sup>Bissinger, N. N. and Breuer, T., *Basic Principles - Gas Turbine Compatibility - Intake Aerodynamics Aspects*, Encyclopaedia of Aerospace Engineering, John Wiley & Sons, Ltd., 2010, pp. 1-10.

DOI: 10.1002/9780470686652.eae487

<sup>16</sup>Coling, Y., B. Aupoix, B., Boussuge, J., F., Chanez, F., “Numerical Simulation of the Distortion Generated by Crosswind Inlet Flows”, *18<sup>th</sup> International Symposium of Air Breathing Engines*, ISABE-2007-1210, Beijing, China, 2007.

<sup>17</sup>Kalpakli Vester, A., Örlü, R., and Alfredsson, P. H., “POD Analysis of the Turbulent Flow Downstream a Mild and Sharp Bend,” *Experiments in Fluids*, Vol. 56, No. 3, March 2015, pp. 57-71.

DOI: 10.1007/s00348-015-1926-6.

<sup>18</sup>Doorne, C. W. H., and Westerweel, J., “Measurement of Laminar, Transitional and Turbulent Pipe Flow Using Stereoscopic-PIV”, *Experiments in Fluids*, Vol. 42, Dec. 2006, pp. 259–279.

DOI: 10.1007/s00348-006-0235-5

<sup>19</sup>Nelson, M., Lowe, K. T., O'Brien, W. F., and Hoopes, K. M., “Stereoscopic PIV Measurements of Swirl Distortion on a Full-Scale Turbofan Engine Inlet”, *52<sup>nd</sup> AIAA Aerospace Sciences Meeting*, National Harbor, Maryland, USA, 2014.

DOI: 10.2514/6.2014-0533

- <sup>20</sup>Mattern, P., Sieber, S., Dues, M., Caglar, S., Gabi, M., “Simultaneous High Speed Stereo PIV and LDA Measurements in the Highly Transient Vortical Wake of an Axial Fan”, *16<sup>th</sup> International Symposium on Laser Techniques to Fluid Mechanics*, Lisbon, Portugal, 2012.
- <sup>21</sup>Guimarães, T., Lowe, K. T., O’Brien, W., “An Overview of Recent results Using the StreamVane Method for Generating Tailored Swirl Distortion in Jet Engine Research”, *54<sup>th</sup> AIAA Aerospace Sciences Meeting*, AIAA SciTech, AIAA 2016-0534, San Diego, USA, 2016. DOI: 10.2514/6.2016-0534
- <sup>22</sup>Zachos, P., MacManus, D., G., Chiereghin, N., “Flow Distortion Measurements in Convolved Aero Engine Intakes”, *33<sup>rd</sup> AIAA Applied Aerodynamics Conference*, AIAA 2015-3305, Dallas, Texas, USA, 2015.  
DOI: 10.2514/6.2015-3305
- <sup>23</sup>Taylor, J., R., *An Introduction to Error Analysis – The Study of Uncertainties in Physical Measurements*, 2<sup>nd</sup> ed., University Science Books, 1997.
- <sup>24</sup>Roach, P., E., “The Generation of Nearly Isotropic Turbulence by Means of Grids”, *International Journal of Heat and Fluid Flow*, Vol. 8, No. 2, 1987, pp. 82-92.  
DOI: 10.1016/0142-727X(87)90001-4
- <sup>25</sup>Raffel, M., Willert, C.E., Wereley, S.T., Kompenhans, J., *Particle Image Velocimetry – A Practical Guide*, 2<sup>nd</sup> ed., Springer-Verlag, Berlin, 2007.  
DOI: 10.1007/978-3-540-72308-0
- <sup>26</sup>MacManus, D., G., Chiereghin, N., Gil Prieto, D., Zachos, P., “Complex aero-engine intake ducts and dynamic distortion”, *33rd AIAA Applied Aerodynamics Conference*, AIAA 2015-3304, Dallas, Texas, USA, 2015.  
DOI: 10.2514/6.2015-3304
- <sup>27</sup>Bouldin, B., Sheoran, Y., “Inlet Flow Angularity Descriptors Proposed for Use with Gas Turbine Engines”, SAE Technical Paper 2002-01-2919, 2002.  
DOI:10.4271/2002-01-2919.
- <sup>28</sup>Seddon, J., *Intake aerodynamics*, 2nd edition, Blackwell Science, Oxford, 1999.
- <sup>29</sup>Doane, D., P., Seward, L., E., “Measuring Skewness: A Forgotten Statistic?”, *Journal of Statistics Education*, Vol. 19, No. 2, 2011, pp. 1-18.

# Flow distortion measurements in convoluted aero engine intakes

Zachos, Pavlos K.

2016-07-07

Attribution-NonCommercial 4.0 International

---

Pavlos K. Zachos, David G. MacManus, Daniel Gil Prieto, and Nicola Chiereghin. Flow Distortion Measurements in Convoluted Aeroengine Intakes, AIAA Journal, Vol. 54, No. 9 (2016), pp. 2819-2832

<https://dspace.lib.cranfield.ac.uk/handle/1826/10021>

*Downloaded from CERES Research Repository, Cranfield University*